RSC Advances

PAPER

View Article Online
View Journal | View Issue

Cite this: *RSC Adv.*, 2025, **15**, 38470

Ecofriendly method for removal of cadmium ions and synthesis of cadmium oxide nanoparticles using a new generation of amine-functionalized cellulose

Dina Hajjar,*[a] M. Mohery *[b] and Gamal M. A. Mahran [c]

We present a new-generation, amine-decorated cellulose adsorbent (CDAM) engineered to overcome the inherent limitations of unmodified cellulose in the sequestration of heavy metals. By covalently grafting branched amine functionalities onto a crosslinked cellulose network, CDAM introduces a dense array of nitrogen-donor sites and enhanced porosity, as confirmed by FTIR (appearance of –NH– peaks), XPS (shifts in N 1s indicating quaternary and imine nitrogen), TGA (improved thermal stability), $^{1}H/^{13}C$-NMR (chemical shifts consistent with successful grafting), and GC-MS (molecular fragmentation patterns). This tailored surface chemistry enables CDAM to achieve a record-high Cd^{2+} adsorption capacity of 483.7 mg g^{-1} under optimized conditions (pH 5.5, 30 min contact, 298 K), substantially outperforming benchmark bio-sorbents. Kinetic studies reveal a pseudo-second-order mechanism, indicative of chemisorption, while equilibrium data conform closely to the Langmuir isotherm, demonstrating monolayer coverage on a homogeneous set of active sites. Thermodynamic analysis ($\Delta H° = +10.4$ kJ mol^{-1}, $\Delta S° = +53$ J mol^{-1} K^{-1}, $\Delta G° < 0$) confirms that Cd^{2+} uptake is endothermic, entropically driven, and spontaneous, with increased randomness at the solid–liquid interface due to desolvation effects. High-resolution XPS of Cd-loaded CDAM shows the emergence of Cd 3d peaks at 405.1 eV and 411.9 eV alongside shifted N 1s binding energies, directly validating metal coordination to imine and amine nitrogen. CDAM exhibits excellent reusability, retaining over 90% of its initial capacity after seven adsorption–desorption cycles with 0.25 M HCl elution, highlighting its practical viability. In a real-world demonstration, CDAM was deployed to treat acid leachates from cadmium-rich Wadi Um-Gheig rock samples. Quantitative Cd^{2+} recovery was achieved, and the purified metal ions were subsequently transformed into high-purity CdO nanoparticles. The resulting CdO exhibits a crystalline monoclinic structure (XRD), uniform nanorod morphology (TEM), and a surface area of 58.4 m^2 g^{-1} (BET), illustrating the dual role of CDAM in environmental remediation and resource valorization. These findings position CDAM as a sustainable, high-performance platform for cadmium removal and value-added nanoparticle synthesis, with broad implications for water treatment and circular-economy strategies.

Received 22nd August 2025
Accepted 22nd September 2025

DOI: 10.1039/d5ra06257h

rsc.li/rsc-advances

1. Introduction

Potentially toxic metals, such as cadmium (Cd), are an essential environmental concern due to their high toxicity, long-lasting presence in the environment, and established carcinogenic and toxicological effects. Cadmium can enter aquatic systems through multiple anthropogenic pathways, including industrial discharge, electroplating processes, battery manufacturing, phosphate fertilizer runoff, and improper disposal of municipal and hazardous waste. Its widespread industrial application, high solubility, and mobility in aqueous systems facilitate its rapid dispersion in surface and groundwater bodies. Cadmium exposure, even at trace levels, has been linked to serious health complications, including nephrotoxicity, pulmonary dysfunction, osteomalacia, and an augmented risk of lung and prostate cancers. Cadmium, a non-essential heavy metal, poses a significant hazard due to its bioaccumulative properties, its non-biodegradability, and its strong affinity for biological tissues.[1] Once released into the environment, Cd^{2+} ions readily migrate from water into agricultural soils, where they can be taken up by crops such as cereals and vegetables, ultimately entering the food chain.[2,3] Prolonged dietary intake of cadmium-contaminated food or water can lead to toxic accumulation in vital organs, causing irreversible damage to the respiratory,

[a]*Department of Biochemistry, College of Science, University of Jeddah, Jeddah 80327, Saudi Arabia. E-mail: dhajjar@uj.edu.sa*

[b]*Department of Physical Sciences, College of Science, University of Jeddah, Jeddah, Saudi Arabia. E-mail: mmohery@uj.edu.sa*

[c]*Mining Engineering Dept., Faculty of Engineering, King Abdulaziz University, Jeddah 21589, Saudi Arabia*

nervous, and digestive systems.[4,5] Due to its high toxicity and strong environmental persistence, cadmium contamination in water bodies has developed as a pressing concern, particularly in areas undergoing rapid industrial growth and intensified agricultural activities. Therefore, the need for efficient and sustainable methods to remediate cadmium-polluted water bodies has become a top priority in environmental research. Cadmium, like many other hazardous heavy metals, is commonly present in industrial wastewater originating from a range of activities, including but not limited to mining operations, metal smelting processes, pigment and dye production, electroplating industries, nuclear power generation, and the manufacturing of textiles. One of the significant environmental challenges associated with cadmium is its high solubility in water, which facilitates its easy dispersion through aquatic systems. This perseverance facilitates cadmium accumulation in marine ecosystems and terrestrial soils, posing serious and long-lasting risks to ecological health and human well-being through the food chain and water supply systems.[6–8]

Its potential to bioaccumulate in trophic chains and its greater solubility in water compared to many other heavy metals make it particularly challenging to remove from contaminated environments. Therefore, developing environmentally benign, cost-effective, and efficient treatment technologies is essential.

Among existing remediation techniques, adsorption has gained prominence because of its simplicity, high effectiveness at low metal concentrations, cost-effectiveness, and scalability for industrial applications.[9,10] Among the various remediation techniques available, adsorption has gained prominence due to its simplicity, high efficiency, cost-effectiveness, and potential for industrial scalability, even when metal concentrations are low.[11–13] While effective, they often suffer from drawbacks such as high reagent consumption, sludge generation, membrane fouling, and high energy demands. In contrast, adsorption offers greater flexibility in adsorbent design and regeneration, making it particularly attractive for heavy metal removal.[14–18]

Many sorbent materials have been explored to remove cadmium from aqueous environments, including industrial byproducts such as red mud and fly ash, naturally occurring compounds like iron oxides, and advanced materials such as organoceramic composites. Bio-waste-derived adsorbents—such as those produced from rice husks, date pits, and other agricultural residues—have garnered considerable attention due to their cost-effectiveness and environmental sustainability.[19–21] Despite these efforts, many of these materials present notable limitations: some display insufficient selectivity toward Cd^{2+} ions, while others suffer from relatively low adsorption capacities or poor reusability following desorption cycles, thereby limiting their practical application in long-term water treatment operations.[22–25]

In contrast, biopolymer-based sorbents, particularly those derived from cellulose and its chemical derivatives, have emerged as promising alternatives. Their natural abundance, biodegradability, and inherent capacity for chemical modification make them attractive candidates for developing customized adsorption systems. Introducing specific functional groups onto the cellulose backbone—such as amines, carboxyls, or phosphates—enhances their binding affinity toward heavy metal ions like Cd^{2+}. Furthermore, the renewable nature of cellulose-based materials aligns well with the growing demand for green and sustainable technologies in water purification. As such, cellulose and its modified forms are increasingly recognized for their potential to address traditional adsorbents' drawbacks and provide scalable, efficient solutions for cadmium remediation.

Cellulose is the most abundant natural polymer on Earth, sourced from various organisms, including plants, marine life, algae, and bacteria. Chemically, it is a linear polymer comprised of D-glucose units connected by $\beta(1 \rightarrow 4)$-linked D-glucose units. It is widely present in plant biomass, such as cotton, wood, and agricultural residues. Despite its abundance and biodegradable nature, raw cellulose exhibits limited effectiveness in adsorbing heavy metals due to its surface's lack of strong binding sites.[26] Thus, the chemical modification of cellulose has become a vital strategy for enhancing its performance as an adsorbent material, particularly for removing heavy metal ions from solutions. Introducing functional groups like amine, carboxyl, thiol, and Schiff bases onto the cellulose backbone can significantly improve its affinity for various metal ions. These functional groups create active sites that facilitate stronger interactions with pollutants, enhancing adsorption efficiency. Additionally, cellulose materials that have been modified in this way demonstrate improved properties, such as greater water stability, increased mechanical strength, expanded surface area, and heightened chemical reactivity. These enhancements boost adsorption performance and position modified cellulose as a promising candidate for various environmental remediation applications, especially in industrial wastewater treatment.[27–30] Modified cellulose materials also exhibit desirable characteristics, including improved water stability, mechanical strength, surface area, and reactivity, making them well-suited for environmental applications.

This innovative design exploits the synergistic effects of a crosslinked cellulose backbone for stability, Schiff base (C=N) moieties for strong chelation, and the introduction of branched, multi-dentate polyamine (triethylenetetramine) functionalities to create a high density of nitrogen-donor sites. This combination is engineered to overcome common limitations of earlier modifications, such as low site density or poor stability, resulting in a record-high adsorption capacity for Cd^{2+}. Furthermore, this study extends beyond remediation by demonstrating a circular-economy approach: the subsequent valorization of the captured cadmium into high-purity CdO nanoparticles, a valuable functional material.

The present study introduces a novel cellulose-network-based adsorbent functionalized with Schiff base and branched amine moieties, creating a high-performance adsorbent for Cd(II) adsorption. This innovative design exploits the synergistic effects of the cellulose backbone, Schiff base coordination sites, and the introduction of quaternary amine functionalities to enhance metal-binding efficiency. The chemical and physical characteristics of the synthesized adsorbent were thoroughly analyzed using many tools such as FTIR, X-ray, XPS, ^{13}C-NMR, H-NMR, and mass spectrometry to confirm successful

functionalization. The adsorption behavior of the new material was systematically investigated against synthetic Cd(II) solutions and real environmental samples collected from the Wadi Um-Gheig region—a geologically significant area between El-Qusier and Ras Banas, known for its mineral-rich rock formations. Moreover, the adsorbed cadmium was successfully recovered and thermally converted into cadmium oxide (CdO) nanoparticles, with their structure, crystallinity, and morphology evaluated using XRD, scanning electron microscopy, and transmission electron microscopy. This dual-purpose strategy enables the effective remediation of toxic cadmium from natural samples. It offers a pathway for resource recovery and value-added nanoparticle synthesis, demonstrating environmental and technological innovation.

2. Materials and methods

2.1. Materials

The analytical-grade chemicals employed in this study included triethylenetetramine (TETA, 99%), cellulose, NaOH (98%), urea (99%), and hydroxylamine hydrochloride (NH_2OH HCl, 99.5%). 1,2,7,8-Diepoxyoctane was obtained from Sigma-Aldrich. Ethanol, acetic acid, and salt of cadmium chloride ($CdCl_2$, 99%) were purchased from Alfa Aesar, USA. Additionally, PEG-4000, HCl, and polyethylene glycol (98%) were purchased from Sigma-Aldrich. A Cd standard solution (1000 mg L^{-1} Cd^{2+}) was manufactured by accurately weighing a suitable amount of $CdCl_2$, dissolving it in 10 mL of 36.5% hydrochloric acid, and diluting the solution to 1 L with purified deionized water.

2.2. Synthesis of aminated cross-linked cellulose CDAM

Cross-linked cellulose beads were synthesized following a methodology described in prior literature.[31] Initially, 2 g of cellulose was stirred in 90 mL of ionized water and 8 g of NaOH (8 g; 0.2 mol), adjusting the pH to 10. Then, 7 g of a 1,2,7,8-diepoxyoctane solution was added to the mixture, which was refluxed for four hours at 200 rpm and 60 °C. The resulting cross-linked cellulose was thoroughly washed with distilled water to exclude residual unreacted diepoxyoctane.

The modified cellulose CDAM was then obtained by reacting the cross-linked cellulose with triethylenetetramine in the presence of carbonyl diimidazole as a catalyst in dimethylformamide under reflux for 10 h at 80 °C. The obtained CDAM was then separated and rinsed many times with distilled water. Finally, the newly synthesized sorbent was dried by placing it in a laboratory oven set at 70 °C for four hours. This step was essential to remove residual moisture and stabilize the material, ensuring its structural integrity and readiness for subsequent characterization and adsorption experiments—Scheme 1.

The interaction mechanism is summarized as a flow. The reaction begins when carbonyl diimidazole (CDI) activates the cellulose hydroxyls by converting –OH groups into reactive imidazolyl carbonates, releasing imidazole as a byproduct. Next, the multi-amine molecule triethylenetetramine (TETA) performs a nucleophilic attack on the electrophilic carbonate carbon, displacing the imidazole and forming stable carbamate (–NH–CO–O–) linkages that tether TETA to the cellulose

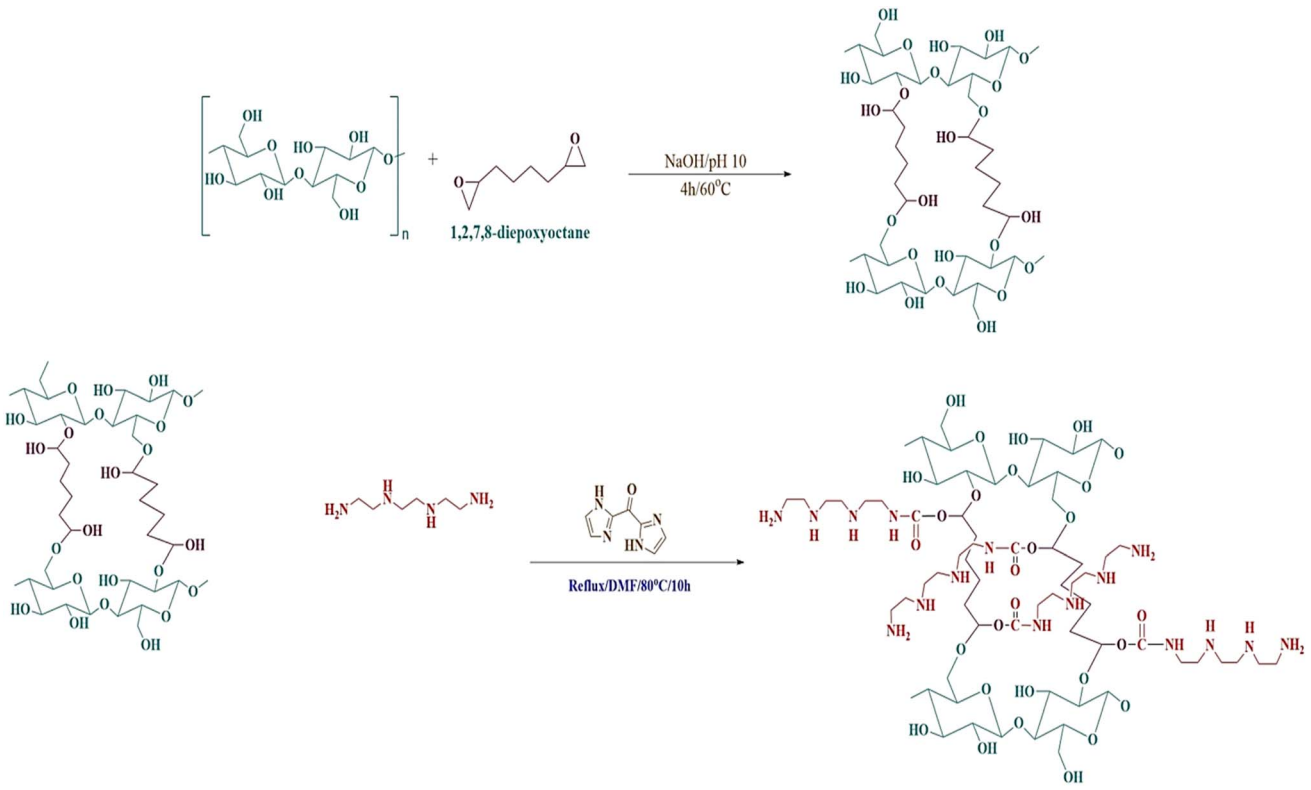

Scheme 1 Synthesis of the CDAM adsorbent.

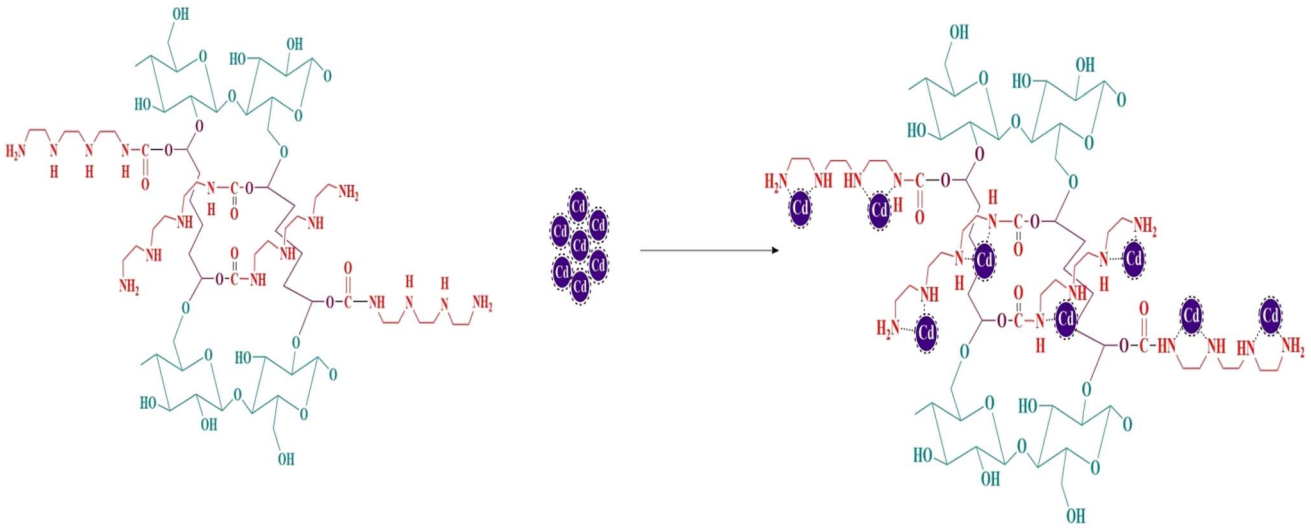

Scheme 2 Interaction mechanism between Cd^{2+} ions and CDAM adsorbent.

backbone. Because TETA contains several amine sites, this coupling can repeat at multiple points, introducing branching or crosslinking depending on the CDI-to-TETA ratio. The entire process is carried out in DMF at 80 °C for around 10 hours, ensuring efficient attachment of the amine groups to the polysaccharide network.

2.3. Sorption evaluations

Experiments in the batch technique were done at 298 K to examine the adsorption capability of the newly prepared CDAM for cadmium ions. To control the optimal adsorption conditions, a series of tests was conducted using an isothermal shaker set at 200 rpm. In each test, 0.25 L of 250 mg L^{-1} Cd solution was utilized while varying the amount of CDAM (250–1700 mg), the pH between 1 and 10, the temperature ranging from 298 to 328 K, and the contact time (10–150 minutes). The pH of the solutions was controlled using a Hanna pH meter, and adjustments were made using dilute 0.01 M HCl and NaOH solutions. Once equilibrium was reached, the solid CDAM adsorbent was separated by filtration with filter paper of the type Whatman. The cadmium ion concentrations in the filtered and initial solutions were measured using an ICP-AES. The equilibrium removal efficiency was mathematically calculated *via* the following:

$$\text{Adsorption } (\%) = \frac{C_{in} - C_{eq}}{C_{in}} \times 100 \quad (1)$$

In this equation, C_{in} and C_{eq} represent the initial and equilibrium concentrations of Cd^{2+} in the liquid phase (mg L^{-1}), respectively. The equation was also utilized to calculate the adsorption capacity, q_e (mg g^{-1}), which indicates the amount of Cd^{2+} adsorbed per gram of CDAM sorbent at equilibrium conditions.

$$q_e = \frac{(C_{in} - C_{eq})V}{m} \quad (2)$$

where m = amount of CDAM sorbent in grams, and V = volume of solution in liters.

2.4. Desorption estimations

2.4.1. Batch adsorption tests. The standard adsorption method involved adding 0.06 g of adsorbent to 20 mL of a 250 ppm Cd^{2+} solution with an initial pH of 5.5 in a conical flask. This mixture was agitated at 200 rpm for 30 minutes at 25 °C, then filtered through filter paper. The Cd^{2+} concentration in the filtrate was analyzed using inductively coupled plasma-atomic emission spectrometry (ICP-AES). The study examined the effects of various factors affecting adsorption efficiency, including initial Cd^{2+} concentration, amount of adsorbent, pH, temperature, and contact time.

The desorption experiments were conducted under carefully controlled conditions to ensure accurate and reproducible results. These conditions were selected based on preliminary optimization studies to maximize desorption efficiency while preserving the structural integrity of the sorbent material. In these studies, 100 mL of a 250 ppm Cd^{2+} solution (initial pH 5.5) was placed in a conical flask, and 150 mg of adsorbent was added. The mixture was shaken at 150 rpm for 30 minutes at 298 K, then filtered through filter paper. The recovered adsorbent was thoroughly washed with HCl and ultrapure water until no Cd^{2+} was detected in the rinse solution, followed by drying in an oven. This dried adsorbent was then used for the next adsorption cycle. The solution concentration was adjusted to 1.5 mg mL^{-1} relative to the adsorbent amount, and the process was repeated for nine cycles. The durability efficiency of the improved cellulose was assessed by measuring the percentage of Cd^{2+} removal after each cycle. All adsorption tests were conducted in triplicate, with results reported as standard deviations. Experimental parameters remained consistent throughout all cycles: initial Cd^{2+} concentration of 250 mg L^{-1} at pH near 5.5, temperature at 298 K, dosage of CDAM is 0.08 g, and a contact time of 30 minutes.

3. Results and discussion

3.1. Characterization

3.1.1. FTIR investigation. The FTIR spectra, in Fig. 1 of the amino-functionalized cellulose derivative (violet) and unmodified cellulose (red), exhibit shared and unique features, confirming successful modification. In both spectra, a broad band around 3400 cm^{-1} corresponds to O–H stretching of hydrogen-bonded water, and the peak near 2900 cm^{-1} arises from C–H stretching in the cellulose backbone, indicating that the polysaccharide framework remains intact after derivatization.[31,32] Characteristic cellulose absorptions at ~1200 cm^{-1} (C–O–C glycosidic linkages) and 1070 cm^{-1} (C–C skeletal vibrations) also persist, albeit with slight shifts in position or intensity, further demonstrating retention of the pyranose ring structure. In contrast, the modified cellulose reveals several new bands between 1300 and 1700 cm^{-1}: the appearance of an N–H bending mode at ~1567 cm^{-1} and a C–N/N–H deformation at ~1475 cm^{-1} confirm primary amine incorporation,[33,34] while a distinct absorption at ~1640 cm^{-1} is attributed to C=N or C–N stretching from Schiff-base or crosslinking reactions. Additional new peaks at 1163 and 1058 cm^{-1} are assignable to C–N vibrations,[35] and the band at 1732 cm^{-1} confirms the presence of carbonyl groups (C=O) introduced during the functionalization process.[36] Together, these spectral changes unambiguously demonstrate that amine groups have been grafted onto the cellulose matrix without compromising its core structure, thus endowing the material with active sites for enhanced adsorption of pollutants or metal ions.

3.1.2. CHNSO elemental analysis. The synthesis CDAM material (816.46 g mol^{-1}) underwent CHNSO elemental analysis, yielding the following practical values: C, 64.95%; H, 8.10%; O, 31.25%; and N, 13.70%. These values closely matched the theoretical values calculated for the $[C_{32}H_{64}N_8O_{16}]_n = 1$ building unit: C, 64.93%; H, 8.12%; O, 31.26%; and N, 13.68%. The strong agreement between experimental and theoretical results confirms the successful synthesis of the target material.

3.1.3. Thermal stability of modified cellulose adsorbent (CDAM). Thermal stability is a crucial property for effectively applying an adsorbent. Thermogravimetric analysis (TGA) was performed to measure the thermal stability of the samples over a temperature range from ambient temperature to 800 °C.[37] As shown in Fig. 2A, microcrystalline cellulose exhibited negligible weight loss below 200 °C. In contrast, modified cellulose slightly reduced weight due to the evaporation of crystallized and physically adsorbed water. Between 200 °C and 500 °C, significant pyrolysis occurred, resulting in weight losses of 83% for cellulose and 55% for modified cellulose. As the temperature increased to 800 °C, carbonization occurred, with total weight losses reaching 87% for cellulose and 65% for modified cellulose. The modified cellulose exhibited a higher thermal decomposition temperature and reduced weight loss, indicating superior thermal stability compared to unmodified cellulose. This enhanced stability may originate from the presence of C=O and C–N bonds in the modified structure, which require more energy to break.[38]

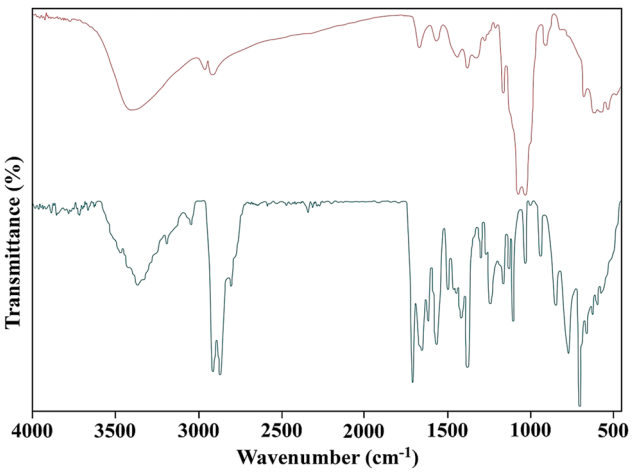

Fig. 1 FTIR analysis of (red) cellulose, (green) CDAM.

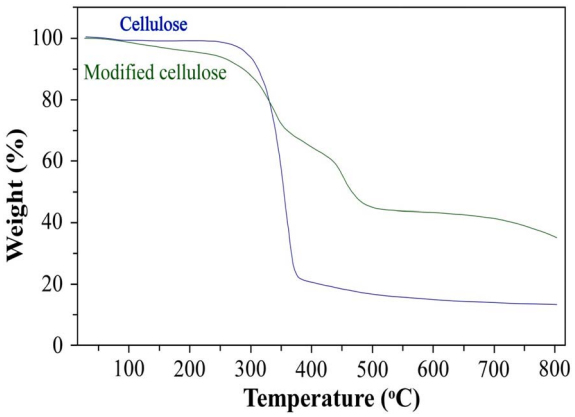

Fig. 2 TGA analysis of cellulose and CDAM.

3.1.4. XPS analysis of CDAM material. The full-spectrum XPS survey scan (Fig. 3a) proves the presence of carbon (C), nitrogen (N), and oxygen (O) in both pristine CDAM and Cd-loaded CDAM composites. A distinct Cd3d peak emerges in the spectra of Cd-adsorbed samples, unequivocally demonstrating the successful uptake of Cd(II) by the adsorbents (C-ATP, C-ATP-SO_4^{2-}, and C-ATP-Cl^-).

High-resolution spectra provide further mechanistic insights:

(1) N 1s spectrum (Fig. 3a): The binding energy of the $-NH_2$ group shifts from 399.8 eV (pristine CDAM) to 400.6 eV post-adsorption, indicative of nitrogen's coordination with Cd(II) through lone-pair electron donation.

(2) O 1s spectrum (Fig. 3a): The binding energy of the –CO–NH_2 moiety increases from 532.4 eV to 533.3 eV after Cd(II) adsorption, corroborating the involvement of both N and O atoms in Cd(II) chelation.[39]

The Cd3d high-resolution spectrum (Fig. 3b) exhibits two characteristic peaks at 405.23 eV ($Cd3d_{5/2}$) and 411.97 eV ($Cd3d_{3/2}$), consistent with the formation of Cd-containing species such as –OCdOH, $CdCO_3$, or $Cd(OH)_2$. These results collectively validate the effective adsorption of Cd(II) onto

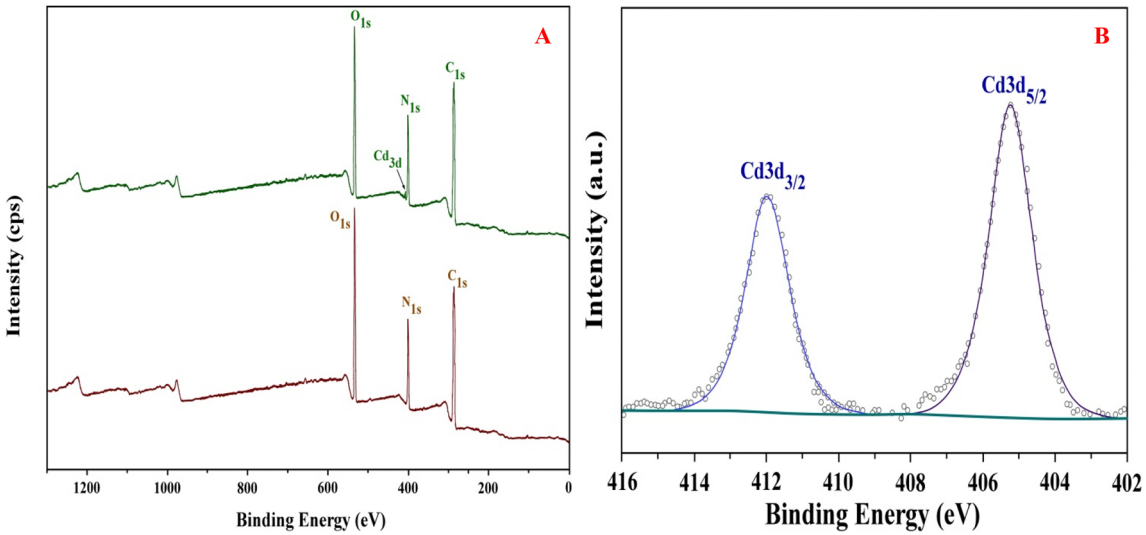

Fig. 3 XPS results of CDAM: (A) before and after sorption (full spectra) and (B) after the adsorption of Cd 3d.

CDAM, with chemical interactions driven by coordination with N/O functional groups and potential surface precipitation.[40,41]

3.1.5. ^{1}H-NMR analysis. ^{1}H-NMR (400 MHz, DMSO-d_6, 25 °C, TMS) δ, ppm: 4.21–5.99 (s, 1H, –OH, J = 5.17 Hz), 3.5–3.59 (t, 1H, –CH, J = 7.24 Hz), 3.76 (d, 2H, –CH_2–O, J = 3.68 Hz), 1.42–1.77 (m, 2H, –CH_2, J = 7.47 Hz), 5.66 (t, 2H, –CH_2–O, J = 4.49 Hz), 2.59–3.16 (t, 2H, –CH_2–NH_2, J = 5.3 Hz), 3.11 (s, 2H, –CH_2–NH_2, J = 6.33 Hz), 5.76 (s, 1H, O=C–NH–, J = 5.38 Hz).

^{1}H NMR analysis, performed at 400 MHz using DMSO-d_6 as the solvent, proved to be an effective tool for providing detailed information about the proton environment in the synthesized composite, thereby aiding in structural elucidation. Two primary assignments represent the pyranose ring and the cross-linked branch containing amine groups. In the pyranose moiety, obvious assignments appear at 4.21–5.99, 3.5–3.59, and 3.76 ppm, which are related to the hydroxy, methine, and methylene protons attached to the oxygen of the pyranose ring. Also, clear assignments of the cross-linked branch containing amine groups appear at 1.42–1.77, 5.66, and 2.59–3.16 ppm, which are related to different methylene protons located upon the cross-linked branch containing amine groups. Moreover, two distinct assignments were observed, which are associated with the amino groups with higher coupling constants. The amino group attached to the methylene moiety appeared as

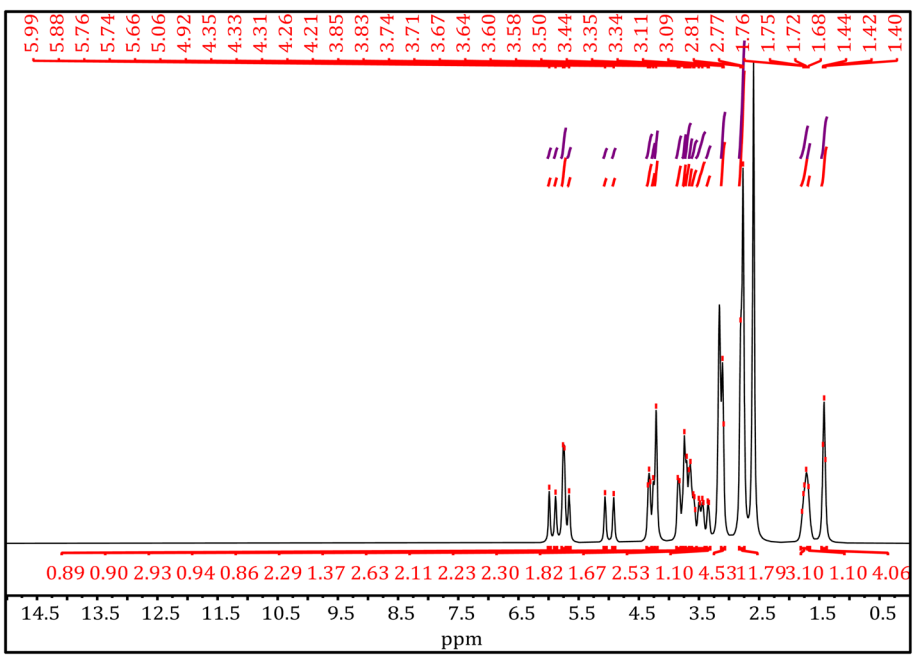

Fig. 4 ^{1}HNMR analysis of CDAM adsorbent.

a singlet at 3.11 ppm (less de-shielded) with a coupling constant of 6.38 Hz. In comparison, the amino group (–NH) attached to the carbonyl moiety appeared at 5.76 ppm (more de-shielded) with a coupling constant of 5.38 Hz. Characterization of the CDAM adsorbent using ^{1}H-NMR is illustrated in Fig. 4.

3.1.6. ^{13}C-NMR analysis. ^{13}C-NMR (100 MHz, DMSO-d_6, 25 °C, TMS) δ, ppm: 70.99–95 (s, 4C, –CH–OH, J = 3.31 Hz), 75.14 (s, 1C, –CH–O–, J = 2.3 Hz), 66.42 (s, 1C, –CH–CH$_2$–O–), 23–33.43 (s, 4C, CH$_2$–), 99.4 (s, 1C, –CH–O–C=O), 39.69–51.8 (s, 6C, –CH$_2$–NH–), 155.61 (s, 1C, –C=O).

^{13}C NMR analysis is a powerful tool for explaining the carbon structure of the synthesized composite. In the case of the synthesized CDAM adsorbent, the spectrum confirms two main structural features: the presence of the pyranose ring and the cross-linked branches containing amine groups. In the pyranose moiety, clear assignments appear at 70.99–95, 75.14, and 66.42 ppm, which are correlated to the methine attached to the hydroxyl group and the oxygen atom, respectively, besides a methylene carbon attached to the oxygen. Also, obvious assignments for the cross-linked branch containing amine groups appear at 23–33.43, 39.69–51.8, 99.4, and 155.61 ppm, which are related to different methylene carbon locations through the cross-linked branch containing amine groups. Moreover, two distinct assignments were observed, which are related to the methylene carbon connected to the –NH group and the methine carbon attached to the –O–C=O group. Finally, the more deshielded carbonyl carbon was detected at a chemical shift of 155.61 ppm. The structural specification of the synthesized CDAM adsorbent, as determined by ^{13}C NMR analysis, is shown in Fig. 5.

3.1.7. MS analysis of CDAM adsorbent. MALDI-TOF/MS, m/z (% rel): $[m/z]^+$ = 816, 190, 179, 103, 45, 44, 18, and 17. Matrix-assisted laser desorption/ionization time-of-flight mass spectrometry (MALDI-TOF/MS) is considered one of the most powerful analytical techniques for characterizing high-molecular-weight compounds, such as the modified CDAM. Its advantages include high sensitivity, excellent resolution, and suitability for high-throughput analysis. The resulting fragmentation pattern provides valuable insights into the structural characteristics of the studied composite.

Important fragments corresponding to the synthesized composite were identified. A quasi-molecular ion peak at m/z 816, attributed to $[C_{32}H_{64}N_8O_{16}]^{\bullet}$ with a relative abundance of 17%, represents the molecular formula of the composite. Moreover, other fragments which were pointed to the successful synthesis of the composite such as pyranose ring $[C_6H_{11}O_6]^{\bullet}$ with m/z of 179 and relative abundance of 71, and $[H_2O]^{\bullet}$ with m/z of 18 and relative abundance of 34, $[CO_2]^{\bullet}$ with m/z of 44 and relative abundance of 28, and $[NH_3]^{\bullet}$ with m/z of 17 and relative abundance of 12.

Additionally, other fragments were associated to polyamine moiety were observed such as $[CH_5N]^{\bullet}$ with m/z of 31 and relative abundance of 18 (methyl amine), $[C_2H_7N]^{\bullet}$ with m/z of 45 and relative abundance of 39 (ethyl amine), $[C_4H_{13}N_3]^{\bullet}$ with m/z of 103 and relative abundance of 13 (diethyl triamine), $[C_6H_{18}N_4]^{\bullet}$ with m/z of 146 and relative abundance of 18 (triethyl tetramine) and $[C_7H_{18}N_4O]^{\bullet}$ with m/z of 190 and relative abundance of 23 (triethyl amine carboxamide). The explanation of the fragmentation pattern of the CDAM adsorbent *via* MALDI-TOF/MS is shown in Fig. 6.

3.2. Cd^{2+} adsorption using CDAM

CDAM was used to investigate the sorption behavior of Cd^{2+} from a synthetic solution. The effects of factors influencing the process, specifically pH, CDAM dosage, contact time, initial Cd^{2+} concentration, and temperature, on sorption efficiency were scientifically assessed. The adsorption performance of the

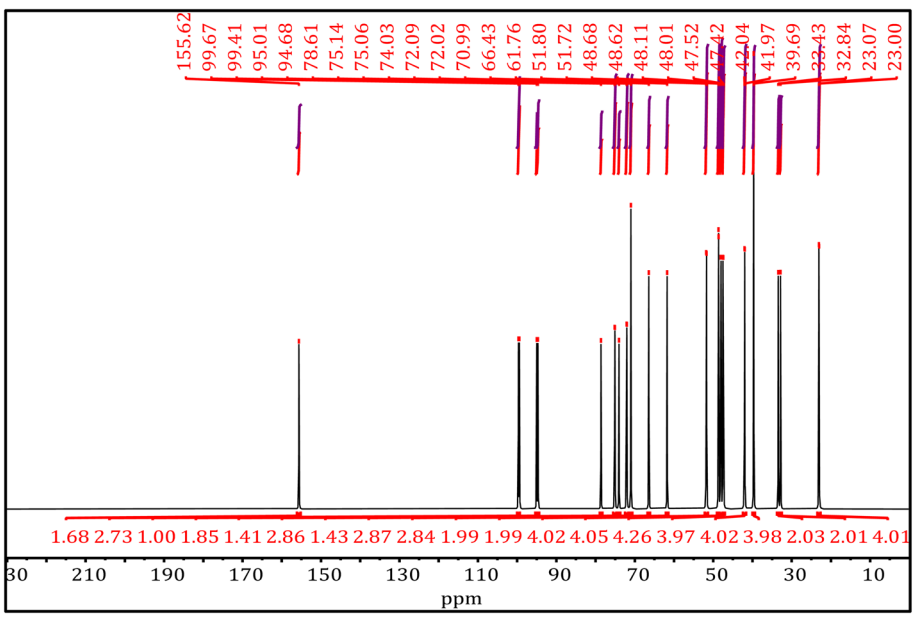

Fig. 5 ^{13}CNMR analysis of CDAM adsorbent.

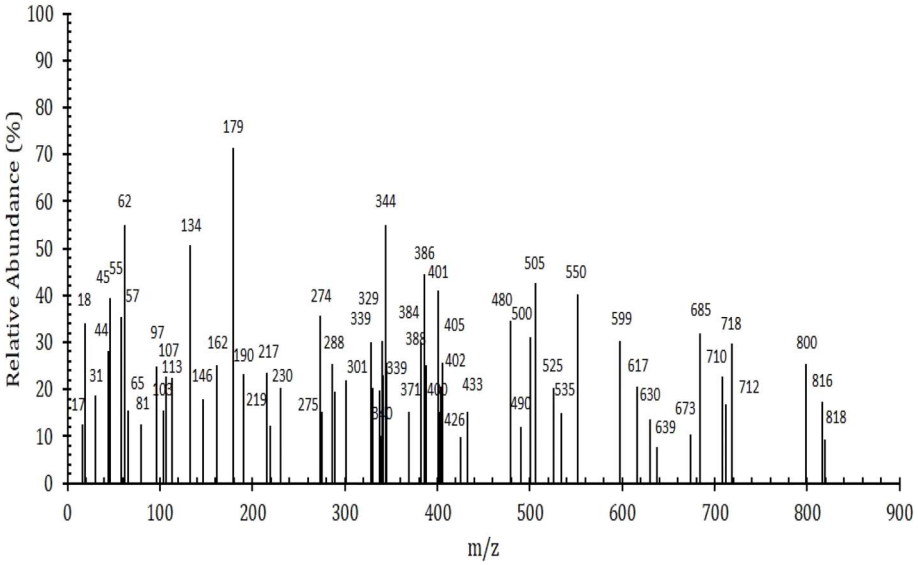

Fig. 6 GC-MS analysis of CDAM adsorbent.

CDAM sorbent for Cd^{2+} ions was systematically evaluated through a series of batch experiments. The key parameters governing the process—solution pH, adsorbent dose, initial Cd^{2+} concentration, contact time, and temperature—were optimized sequentially. The data obtained under these optimized conditions were then modeled using established kinetic, isotherm, and thermodynamic equations to elucidate the adsorption capacity, rate-limiting steps, and underlying mechanism.

3.2.1. Influence of pH on Cd(II) sorption and the role of pH_{pzc}. The Cd(II) sorption efficiency onto the synthesized CDAM material demonstrated a significant dependence on the solution pH, as shown in Fig. 7a. The removal percentage steadily increased from approximately 20% at pH 1 to a peak of nearly 87% at pH 5.5, followed by a gradual decline with further increases in pH. This trend can be attributed to the interaction between the surface charge of the adsorbent material and the aqueous speciation of cadmium ions at varying pH levels.

At low pH values (1–3), the high concentration of (H_3O^+) in the solution results in intense competition with Cd^{2+} ions for available sorption sites. Simultaneously, the surface of the CDAM material is highly protonated under acidic conditions, resulting in a positively charged surface that repels the cationic Cd^{2+} species. Consequently, the adsorption efficiency remains limited in this pH range.

As the pH increases from 3 to approximately 5.5, the concentration of H_3O^+ diminishes, reducing competition and decreasing surface protonation. This transition enhances the electrostatic attraction between the adsorbent surface and Cd^{2+} ions. The significant enhancement in sorption observed in this region is further explained by the material's point of zero charge (pH_{ZPC}), which was experimentally determined to be about 4.6, as shown in Fig. 7b. Below this pH, the surface bears a net

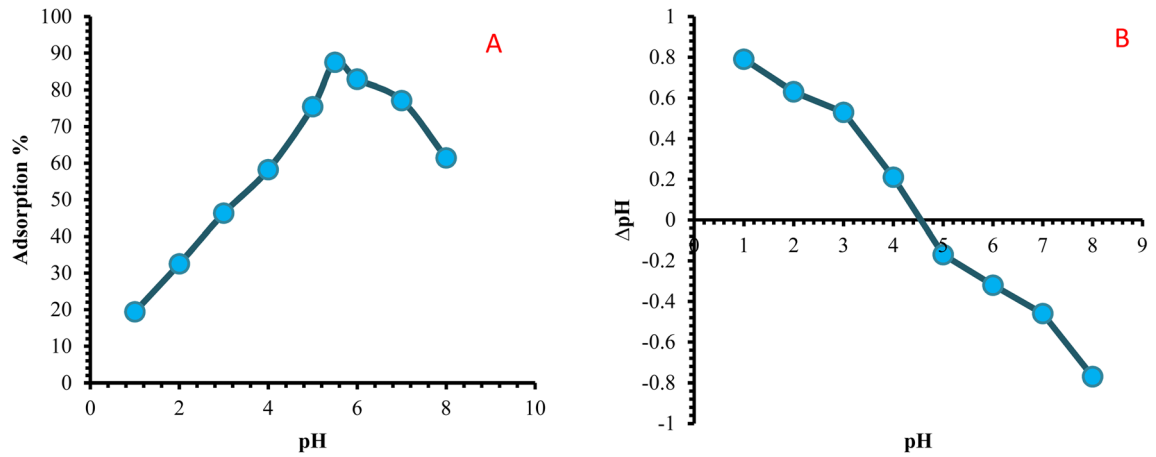

Fig. 7 (A) Impact of pH on the sorption of Cd^{+2} using CDAM, (B) pH_{ZPC} of the CDAM adsorbent. Cd^{+2} concentration, 250 mg L; CDAM dose 0.1 g; equilibration time, 20 min, and temperature, 30 °C.

positive charge. In contrast, above $pH_{ZPC,}$ the surface becomes increasingly hostile. Thus, at pH values above 4.6, the negatively charged surface favors the uptake of Cd^{2+} ions *via* electrostatic interactions and possibly through complexation with surface functional groups such as carboxylate, phosphate, or hydroxyl moieties.

The maximum adsorption efficiency observed near pH 5.5 corresponds to conditions where the surface of the adsorbent is sufficiently deprotonated and negatively charged, and cadmium ions predominantly exist as free Cd^{2+} species in solution. Above this pH, the gradual decline in adsorption capacity is likely due to the formation and precipitation of cadmium hydroxide as the concentration of hydroxide ions (OH^-) increases. This precipitation removes Cd^{2+} ions from the solution through a process other than adsorption, consequently lowering the observed adsorption capacity.

The best pH range for Cd(II) adsorption onto CDAM lies above the material's pH_{pzc}, where the surface charge transitions to negative and electrostatic attraction toward Cd^{2+} ions is maximized. These findings underscore the significant influence of the adsorbent's surface characteristics and the chemical forms of metal ions in solution on adsorption. Consequently, optimizing the pH is essential for successfully using this material to remove heavy metals from its solutions.

3.2.2. Effect of adsorbent dose. The adsorbent's mass is crucial in adsorption studies, as it directly influences the number of active binding sites available for capturing dissolved metal ions. To systematically explore this effect, we conducted a series of batch experiments where the CDAM sorbent dosage varied between 0.5 and 3.0 g L^{-1}, while keeping all other operational parameters constant: the initial cadmium ion concentration was maintained at 250 mg L^{-1}, the solution pH was buffered at 5.5, the temperature was kept at 20 °C, and the suspension was stirred for 30 minutes. As illustrated in Fig. 8, gradually increasing the sorbent mass—from 0.01 g to 0.06 g per 100 mL sample—led to a significant enhancement in removal efficiency, with the percentage of Cd^{2+} ions extracted increasing from around 40 percent to over 80 percent. This improvement is due to the higher ratio of available adsorption sites compared to the number of metal ions, facilitating more frequent collisions and binding events.

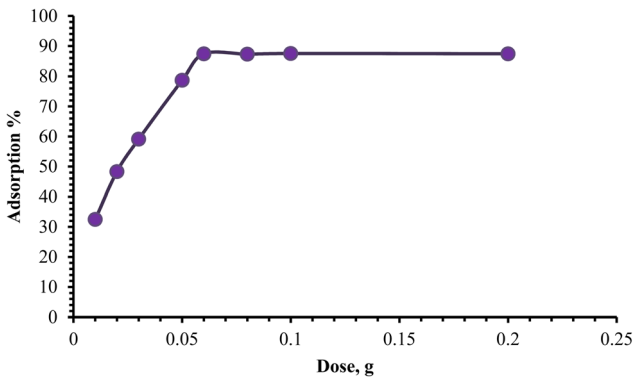

Fig. 8 The impact of adsorbent dose on the sorption process of Cd^{+2} by the CDAM.

Beyond the 0.06 g threshold, however, further increases in sorbent mass yielded only marginal gains in cadmium uptake, indicating that the system had approached site-saturation under the given conditions. At this plateau, nearly all accessible functional groups on the CDAM surface were occupied, and additional material contributed redundant binding capacity. Based on these observations, 0.06 g per 100 mL (equivalent to 0.6 g L^{-1}) was selected as the optimal dose for subsequent kinetic, isotherm, and thermodynamic experiments, balancing maximal removal performance with material efficiency. This optimized dose ensures that adsorption trials proceed under conditions where capacity is sufficiently exploited without excess sorbent material.

3.2.3. Influence of contact time and kinetic modelling of Cd^{2+} sorption onto CDAM. Understanding how adsorbents behave over time is crucial for designing effective and economically viable leach liquor systems that can be scaled up for commercial use. In this research, the rate at which cadmium ions (Cd^{2+}) were adsorbed onto the synthesized cellulose-based amine-modified adsorbent (CDAM) was studied at 298 K, using a 250 mg L^{-1} (Cd^{2+}) concentration, a pH of 5.5, and an adsorbent amount of 0.06 g. As depicted in Fig. 9a, the uptake of (Cd^{2+}) rapidly increased during the initial 30 minutes. This rapid adsorption is likely a result of the abundance of unoccupied binding sites on the sorbent's surface and a significant concentration difference between the bulk solution and the adsorbent surface at the beginning of the process.[42] The sorption rate gradually slowed as the active sites became occupied, reaching equilibrium at approximately 100 minutes. No significant increase in uptake was observed beyond 120 minutes, which was subsequently used as the optimal equilibrium time.

To elucidate the underlying mechanism of Cd^{2+} sorption, the kinetic data were investigated using four widely applied models: pseudo-first-order (PFO), pseudo-second-order (PSO), intraparticle diffusion (IPD), and Elovich. The kinetic parameters obtained from the linearized forms of these models are summarized in Table 1.

The PFO model,[43] which operates under the assumption that the rate at which sorption sites are filled is proportional to the number of sites still available, did not accurately reflect the observed experimental results. As shown in Fig. 9b, the linear plot of $\log(q_e - q_t)$ *versus* time displayed a low correlation coefficient (R^2), and the theoretical equilibrium adsorption capacity (q_e, cal) calculated from this model significantly deviated from the experimentally observed value (q_e, exp). These discrepancies suggest that the model was unsuitable for describing how Cd^{+2} was adsorbed onto CDAM, likely because the interaction between the adsorbent and the adsorbate involves chemical bonding.

$$\mathrm{Log}(q_e - q_t) = \log q_e - \frac{K_1 t}{2.303} \quad (3)$$

In contrast, the PSO model, which posits that the adsorption rate is limited by chemical bonding, closely matched the experimental data (Fig. 9c). The high R^2 value and the strong agreement between the calculated ($q_{e_{cal}}$) and experimental ($q_{e_{exp}}$)

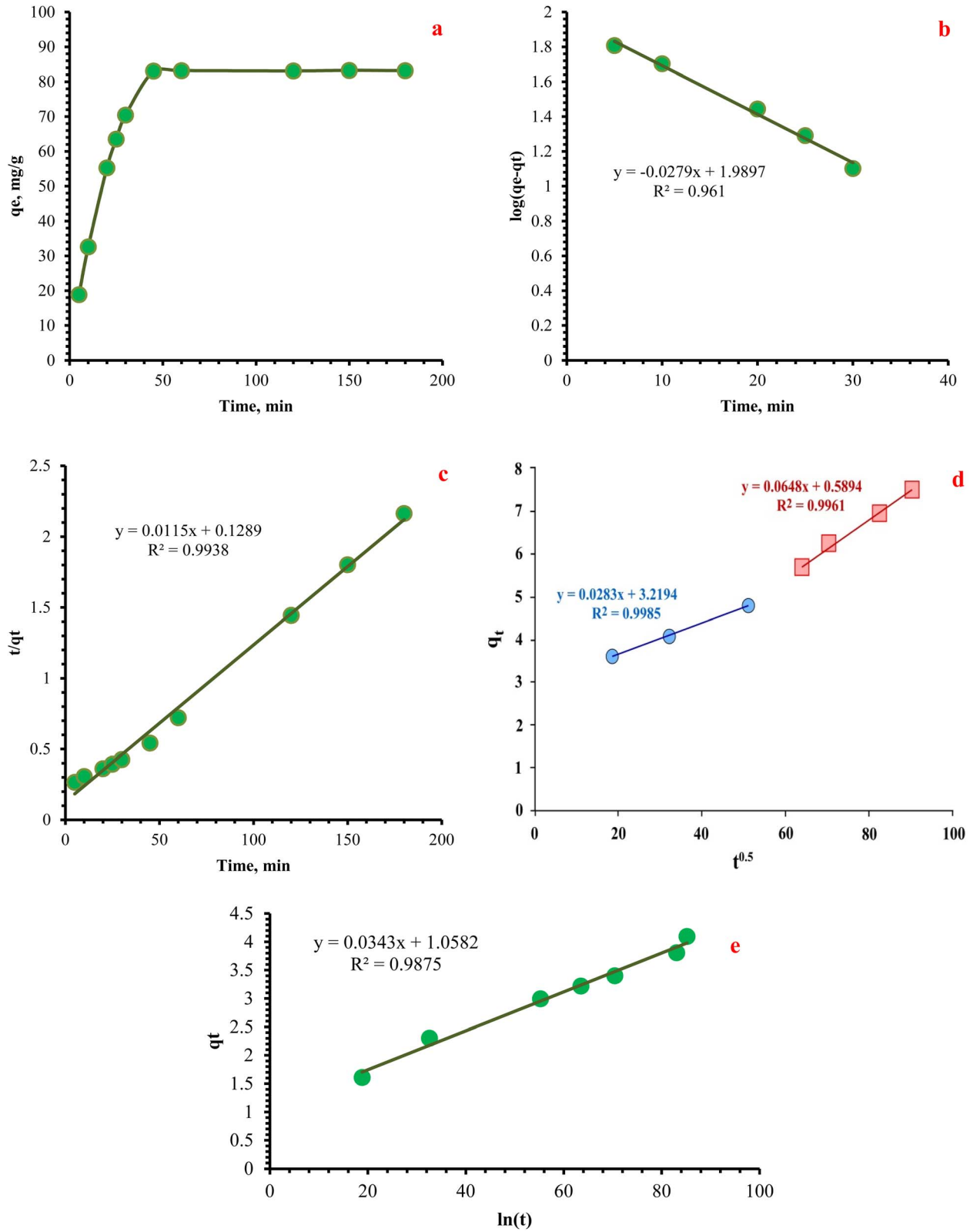

Fig. 9 (a) Time effect of the Cd^{+2} adsorption, (b) pseudo 1st order, (c) pseudo 2nd order, (d) the IPD model, (e) Elovich model of Cd^{+2} adsorption process using CDAM. ([Cd^{+2}] = 250 ppm/20 mL, pH = 5.5, t = 45 minutes, 0.06 g dosage, T = 25 °C, agitation rate = 200 rpm]).

equilibrium adsorption capacities confirm the suitability of the PSO model. The rate constant (k_2) and the sorption capacity derived from this model suggest that the adsorption process is mainly governed by the formation of chemical bonds, such as those between the amine groups on the CDAM and the Cd^{2+} ions, rather than by simple physical attraction.[44,45]

Table 1 Kinetic factors controlling Cd(II) adsorption upon CDAM

1st ordered kinetic				2nd order kinetic			
K_1	$q_{(max)cal}$	R^2	$q_{max(exp)}$	K_2		$q_{(max)cal}$	R^2
0.0643	97.656	0.961	83.04	0.001		86.956	0.9938
Elovich model				Intra-particle diffusion rate model			
α	β	R^2		K_d (mg g^{-1} min$^{-0.5}$)		C	R^2
0.0356	29.155	0.9875		1st stage	0.0283	3.2194	0.9985
				2nd stage	0.0648	0.5894	0.9961

$$\frac{t}{q_t} = \frac{t}{q_e} + \frac{1}{k_2 q_e^2} \quad (4)$$

To further probe the mass transfer mechanisms and rate-limiting steps, the intra-particle diffusion (IPD) model was employed.[46] According to the Weber–Morris equation:

$$q_t = k_d t^{0.5} + C \quad (5)$$

q_t is the quantity of Cd^{2+} sorbed at time t, k_i (mg g^{-1} min$^{-\frac{1}{2}}$) is the diffusion rate constant, and C (mg g^{-1}) is the boundary layer thickness. As depicted in Fig. 9d, the plot of q_t *versus* $t^{\frac{1}{2}}$ yielded a multilinear curve, indicating that intra-particle diffusion is involved in the sorption process but is not the sole rate-determining step. The plot consists of two linear regions: the initial steeper region (k_{i1}) is associated with external surface sorption and boundary layer diffusion. In contrast, the second region (k_{i2}) with a lower slope corresponds to the gradual adsorption within the pores of the adsorbent. The intercept C is non-zero, implying that boundary layer resistance contributes to the adsorption mechanism.[47,48] These results suggest a multi-stage adsorption process involving both external and internal diffusion.

The Elovich model, which describes chemisorption on heterogeneous surfaces, was also applied to assess the kinetics of surface interaction. The equation expresses the model:[49]

$$q_t\left(\frac{1}{\beta}\right)\ln(\alpha\beta) + \left(\frac{1}{\beta}\right)\ln t \quad (6)$$

α (mg g^{-1} min^{-1}) represents the initial sorption rate and β (g mg^{-1}) is associated with the extent of surface coverage and activation energy for chemisorption. The plot of q_t *versus* ln(t) showed a high R^2 value (0.9875), signifying a respectable fit between the experimental data and the model (Fig. 9e). The values of α (0.0356 mg g^{-1} min^{-1}) and β (29.155 g mg^{-1}) reveal that the adsorption process involves heterogeneous energy sites and chemisorption characteristics. Although the Elovich model exhibited strong compatibility with the data, it is more descriptive of surface properties than the adsorption mechanism.

In summary, the sorption kinetics of Cd^{2+} onto CDAM is best defined by the PSO model, confirming that chemisorption is the dominant mechanism, likely involving electron sharing or exchange between Cd^{2+} and amine functional groups on the sorbent surface. However, the intra-particle diffusion and Elovich models also provided meaningful insights. The IPD model demonstrated that film diffusion and pore diffusion play roles in the rate-limiting steps of the process. In contrast, the Elovich model confirmed that chemisorption occurs on a heterogeneous surface. Therefore, while the PSO model offers the most accurate prediction of kinetic behavior, the IPD and Elovich models complement the analysis by revealing the complexity of diffusion and surface interaction phenomena involved in cadmium uptake by CDAM. These findings provide a robust foundation for understanding the adsorption mechanism and optimizing the adsorbent for practical applications in wastewater treatment.

In summary, the sorption kinetics are best defined by the pseudo-second-order model. The high correlation coefficient ($R^2 > 0.99$) and the agreement between theoretical and experimental q_e values confirm that chemisorption is the dominant, rate-limiting mechanism. This likely involves electron sharing or exchange between the Cd^{2+} ions and the nitrogen-based functional groups (amines, imines) on the CDAM surface.

3.2.4. Impact of the initial concentration of metal ions. The adsorption performance of the CDAM sorbent was systematically examined by exposing it to solutions containing increasing cadmium ion concentrations, ranging from 250 to 1700 mg L^{-1}, while maintaining the previously optimized parameters (45 min contact time and pH 5.5). As illustrated in Fig. 10A, the amount of Cd^{2+} captured per gram of CDAM steadily rose as the initial metal concentration increased, reflecting the enhanced mass transfer driving force at higher ion levels. However, upon reaching the maximum concentration of 1700 mg L^{-1}, the adsorption capacity curve leveled off, indicating that the available surface sites of the sorbent had become fully occupied, preventing further uptake. This plateau region arises because, beyond a certain threshold, the limited number of functional groups on the CDAM surface cannot accommodate additional ions, even though the solution contains more Cd^{2+}. At these elevated concentrations, competition among cadmium ions intensifies, and the likelihood of each ion finding an unoccupied binding site decreases, effectively capping the removal efficiency.[50] Nevertheless, the overall trend confirms a strong positive correlation between the initial Cd^{2+} concentration and the sorbent's loading capacity. The increased ionic strength in the solution amplifies the concentration gradient between the bulk phase and the sorbent interface, overcoming boundary-layer diffusion resistances and promoting more frequent collisions with active sites. Consequently, the sorbent achieves its maximum uptake only when the thermodynamic driving force is sufficient to populate nearly

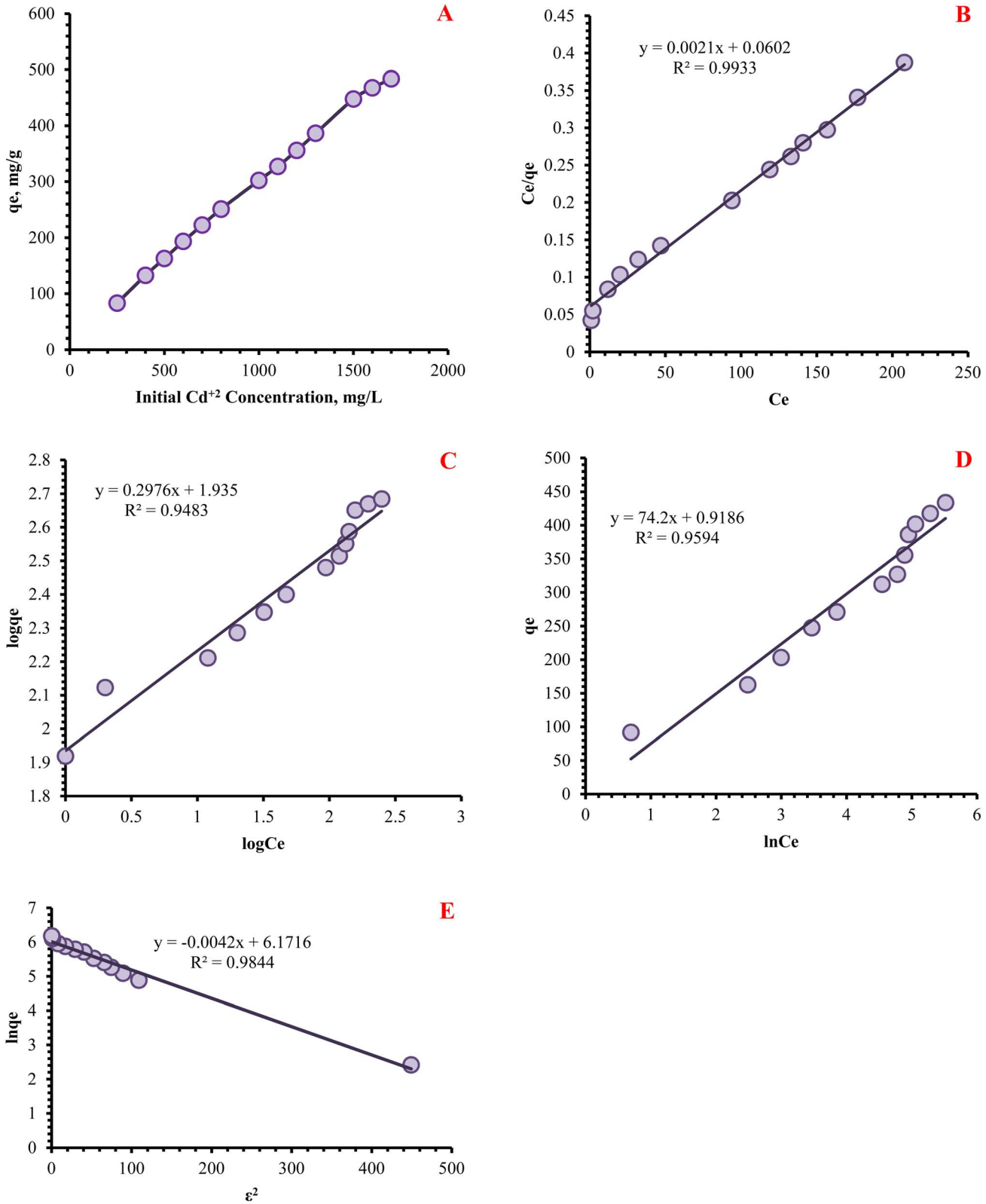

Fig. 10 (A) Initial cadmium concentration, (B) Langmuir, (C) Freundlich, (D) Tempkin, and (E) Dubinin–Radushkevich. Isotherm models of Cd^{+2} ions adsorption using CDAM.

all adsorption sites. This demonstrates the robust performance of the CDAM material in high-concentration removal scenarios.[51] This equilibrium adsorption data, which defines the relationship between the residual concentration in solution and the amount adsorbed on the surface at a constant temperature, is critical for determining the maximum capacity

of the sorbent and understanding the nature of the adsorbate–adsorbent interactions. To this end, the data were analyzed using four fundamental adsorption isotherm models: the Langmuir, Freundlich, Temkin, and Dubinin–Radushkevich (D–R) models.

3.2.5. Adsorption isotherms. Understanding sorption isotherms is crucial for determining the maximum adsorption capacity of a material, which is essential for optimizing practical sorption systems. This study analysed the equilibrium data using four standard isotherm models—Langmuir, Freundlich, Temkin, and Dubinin–Radushkevich. The Langmuir model is based on the premise that sorption occurs uniformly on a homogeneous surface, forming a single layer of adsorbate, and that there are no interactions between the adsorbed molecules. The linearized form of the Langmuir isotherm is given by eqn (7) and Fig. 10B:[52,53]

$$\frac{C_e}{q_e} = \frac{C_e}{q_m} + \frac{1}{q_m K_l} \tag{7}$$

The Freundlich isotherm model describes sorption on heterogeneous surfaces, where the energy of the binding sites varies across the surface (Fig. 10C).[54,55] In contrast, the Temkin isotherm operates on the principle that the heat of adsorption decreases linearly as the surface becomes more covered due to interactions between the adsorbed molecules (Fig. 10D).[56]

$$\text{Log } q_e = \log K_f + \frac{1}{n}\log C_e \tag{8}$$

$$q_e = \frac{RT}{b}\ln A + \frac{RT}{b}\ln C_e \tag{9}$$

In the Langmuir model, K_L represents the association constant of the binding sites (L mg^{-1}), while q_m denotes the theoretical maximum monolayer sorption capacity (mg g^{-1}). C_e is the equilibrium concentration of Cd^{+2} ions in solution (mg L^{-1}), and q_e indicates the equilibrium amount of Cd^{+2} adsorbed per unit mass of CDAM (mg g^{-1}). For the Temkin model, A_T is the binding constant (L g^{-1}), R is the universal gas constant, T is the absolute temperature (K), and b_T reflects the variation of adsorption heat (kJ mol^{-1}).

The Dubinin–Radushkevich (D–R) isotherm is particularly effective in distinguishing between different adsorption mechanisms, such as ion exchange, physical adsorption, and chemisorption, by calculating the mean free energy of adsorption (E). eqn (10),[57,58] Fig. 10E

$$\text{Ln } q_e = \ln q_D - B_D(\varepsilon)^2 \tag{10}$$

Additionally, eqn (11) defines the dimensionless separation factor R_L, which helps predict the nature of adsorption based on the initial Cd^{2+} concentration C_o. The parameter R_L indicates the favorability of adsorption: Values greater than 1 (*i.e.*, $1/n < 1$) indicate favorable adsorption. Values between 0 and 1 (*i.e.*, $1/n > 1$) suggest unfavorable adsorption.[59] The R_L values of this study, ranging from 0.01 to 0.04 for CDAM adsorbents, confirm a highly favorable adsorption process.

Table 2 Sorption isotherm factors controlling several models for Cd^{+2} ions by CDAM[a]

Kinetic models	Parameters	
Langmuir isotherm	Equation	$y = 0.0021x + 0.0602$
	q_{max} (mg g^{-1})	476.19
	K_l	0.0349
	R^2	0. 9933
Freundlich isotherm	Equation	$y = 0.2976x + 1.935$
	K_f (mg g^{-1})	86.099
	$1/n$ (mg min g^{-1})	0.2976
	R^2	0.9483
Tempkin isotherm	Equation	$y = 74.2x + 0.9186$
	A_T (L m^{-1})	1.0124
	b_T	33.39
	R^2	0.9594
D–R isotherm	Equation	$y = -0.0042x + 6.1716$
	q_D (mg g^{-1})	478.95
	B_D (Mo1^2 kJ^{-2})	0.0042
	E_D (kJ mo1^{-1})	10.911
	R^2	0.9844
Practical capacity	q_{exp}	483.67

[a] The strong fit to the Langmuir isotherm ($R^2 = 0.9933$) indicates that adsorption occurs through monolayer coverage onto a surface composed of homogeneous binding sites. The high theoretical maximum capacity (q_m = 476.19 mg g^{-1}), which aligns closely with the experimental value (483.67 mg g^{-1}), underscores the efficacy of the functionalization strategy in creating a high density of uniform sites for Cd^{2+} sequestration.

$$R_l = \frac{1}{1 + K_l C_o} \tag{11}$$

From Table 2, according to Langmuir factors controlling, the extreme theoretical sorption capacity of CDAM reached 476.19 mg g^{-1} at room temperature and pH 5.5. This closely matches the experimental results 483.67, reinforcing that the Langmuir model accurately defines the observed behaviour and that functional group interactions play a vital role in improving sorption capacity.

The Temkin model was also considered; it was effective in fitting the experimental data, likely due to its assumption of heterogeneous surfaces, and indicated by the higher correlation coefficient. In this model, the constant b, related to adsorption heat, was calculated as 33.39 kJ mol^{-1}, while the binding energy (A_T) was determined to be 1.0124 L g^{-1}, as shown in Fig. 10E. Furthermore, the D–R isotherm model provided strong evidence for chemisorption, supported by the calculated mean adsorption energy E of 10.911 kJ mol^{-1} and a high correlation coefficient ($R^2 = 0.9844$). These findings validate the suitability of the D–R model in describing the uptake of Cd^{+2} ions onto CDAM.

3.2.6. Sorption thermodynamics. To better understand how Cd^{2+} ions are adsorbed onto CDAM, thermodynamic parameters were calculated using the van't Hoff plot (Fig. 11). The slope and interception of this plot were used to determine the enthalpy change ($\Delta H°$) and entropy change ($\Delta S°$) using eqn (13). In contrast, the Gibbs free energy change ($\Delta G°$) was calculated using eqn (12) and (13).

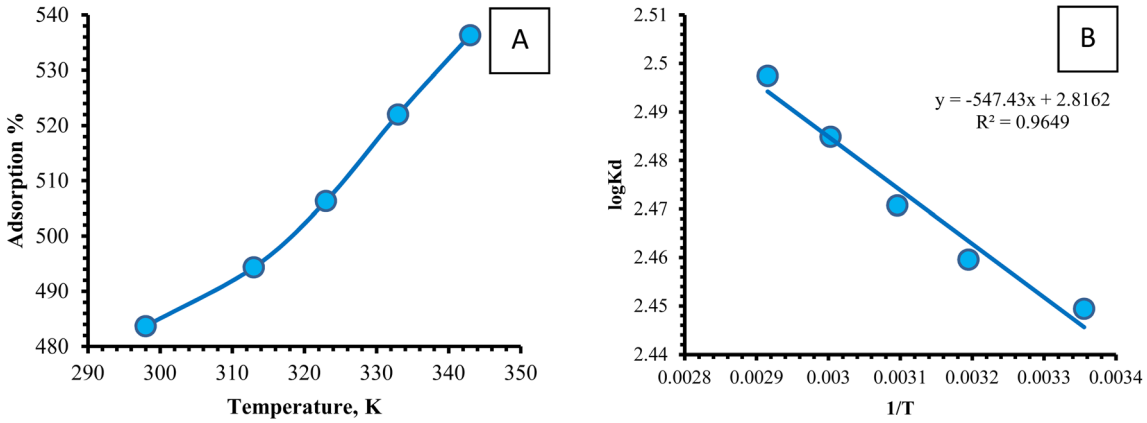

Fig. 11 (A) The effect of temperature on the sorption process of Cd^{+2} ions upon CNT-AMP, (B) plot of log K_d *vs.* $1/T$, of sorption of Cd^{+2} ions upon CNT-AMP adsorbent. ([Cd^{+2}] = 1700 ppm/20 mL, pH = 5.5, t = 45 minutes, 0.06 g dosage, T = 25 °C, agitation rate = 200 rpm]).

Table 3 Thermodynamic factors for Cd^{+2} ions adsorption by CDAM at different temperatures

ΔH° (kJ mol^{-1})	ΔS° (J mol^{-1} K^{-1})	ΔG° (kJ mol^{-1})				
10.482	53.922	298 K	313 K	323 K	333 K	343 K
		−16.058	−16.867	−17.406	−17.946	−18.485

$$\text{Log } K_d = \frac{\Delta S}{2.303R} - \frac{\Delta H}{2.303RT} \quad (12)$$

$$\Delta G^\circ = \Delta H^\circ - T\Delta S^\circ \quad (13)$$

The evaluated thermodynamic constants (ΔG°, ΔH°, and ΔS°) were systematically obtained using the relationships provided in eqn (12) and (13).

The thermodynamic isotherm study examined how temperature (ranging from 298 K to 343 K) affects the adsorption of Cd^{2+} by the CDAM adsorbent. Table 3 presents the characteristics of Cd^{2+} adsorption at these different temperatures. The results showed an apparent increase in sorption capacity as the temperature rose, from 483.70 mg g^{-1} to 536.30 mg g^{-1} (as detailed in Table 3), suggesting that the adsorption process is endothermic, meaning higher temperatures promote the uptake of Cd^{2+} ion.[60,61]

The thermodynamic parameters summarized in Table 3 support the conclusion that chemical interactions are the primary mechanism governing the adsorption process. The enthalpy change (ΔH^0) was 10.482 kJ mol^{-1}, falling within the typical range for chemisorption.[62] The Gibbs free energy values (ΔG^0), ranging from −16.058 to −18.485 kJ mol^{-1}, indicate a spontaneous process, further supporting the presence of chemical adsorption mechanisms.[63] Additionally, the positive (ΔS^0 = 53.922 J mol^{-1} K^{-1}) reflects increased randomness at the solid–liquid interface, which enhances the interaction between the sorbent and Cd^{2+} ions.[64]

Overall, thermodynamic analysis confirms that CDAM exhibits strong chemisorption characteristics, as evidenced by the highest ΔH^0 (10.482 kJ mol^{-1}), most negative ΔG^0 (−18.485 kJ mol^{-1}), and largest ΔS^0 (53.922 J mol^{-1} K^{-1}). These indicate dominant chemical interactions, likely due to coordination with functional groups on the CDAM surface.

The thermodynamic parameters collectively confirm that the adsorption process is endothermic (ΔH° = +10.482 kJ mol^{-1}), spontaneous (ΔG° < 0), and results in an increase in randomness at the solid–liquid interface (ΔS° = +53.922 J mol^{-1} K^{-1}). The positive ΔH° value falls within the typical range for chemisorption, further supporting the mechanism proposed from the kinetic and isotherm analyses.

3.3. Comparing cadmium adsorption on CDAM with other literature

Based on the comparative data presented in Table 4, the synthesized CDAM adsorbent exhibits exceptional cadmium ion removal efficiency, surpassing many previously reported adsorbent materials. With a maximum adsorption capacity of 483.7 mg g^{-1}, CDAM clearly demonstrates a significant improvement over various conventional and advanced sorbents, including modified cellulose derivatives, engineered biochars, and polymer-based composites. This outstanding performance reflects nearly a twofold increase in adsorption capacity compared to materials like carboxymethyl cellulose/polyacrylamide (256.4 mg g^{-1}) and TiO_2/glutaraldehyde/carboxymethyl cellulose (274.28 mg g^{-1}), which are already considered adequate in cadmium removal applications.

Even when compared to high-capacity sorbents such as CTPO (307 mg g^{-1}) and Mg-modified biocarbon (up to 223.7 mg g^{-1}), CDAM demonstrates significantly superior efficiency. This

Table 4 Comparison of Cd^{2+} sorption capacity on CDAM and further sorbents

Adsorbent	Adsorption capacity, mg g^{-1}	Ref.
Silicon and β-cyclodextrin (β-CD) comodified rice husk biochar (β-CD@SiBC)	137.6	65
Mg-modified biocar (Cys@MgBC)	175.9–223.7	66
Canna indica-derived biochar	188.8	67
Carboxymethyl cellulose/polyacrylamide	256.4	68
Ca–Mg phosphate based on dolomite	241.7	69
Methylisothiocyanate decorated PAMAM dendrimer/mesoporous silica	97.8	70
Chelating polyacrylonitrile	146.0	71
TiO_2/glutaraldehyde/carboxymethyl cellulose	274.28	72
CTPO	307	21
Silicate-modified biochar derived from Sawdust	178.58	73
Ultrasonic magnesium-modified biochar (UMBC)	138.5	74
Montmorillonite microwave-assisted acid treatment (4MAT-Mt)	388.32	75
NTW	42.35	76
WHHC-CA1	166.6	77
CDAM	483.7	This study

exceptional performance of CDAM can be attributed to its abundant surface functionalities, especially amine groups, which provide strong coordination sites for Cd^{2+} ions. Furthermore, the sorbent's well-developed porous structure enhances mass transfer by offering a large surface area and accessible diffusion pathways, which together enable rapid and efficient metal uptake.

The remarkable enhancement in sorption capacity is directly attributed to the tailored surface functionalization strategy employed in the preparation of CDAM. This strategic modification not only increases the number of effective adsorption sites but also enhances the material's affinity for cadmium ions. Combined, these structural and chemical advantages position CDAM as a highly effective and competitive candidate for real-world wastewater treatment applications, particularly those targeting cadmium contamination in industrial effluents. The data strongly support CDAM's potential to surpass traditional sorbents in efficiency and practical utility. *Even when compared to these recent and high-performing adsorbents, CDAM demonstrates a significantly superior adsorption capacity, nearly doubling the performance of many materials reported in the last two years.*

3.4. Impact of coexisting ions upon the sorption of Cd^{2+}

The influence of coexisting metal ions on the selective uptake of Cd^{2+} by the CDAM sorbent was thoroughly investigated under optimized experimental conditions. This assessment was crucial for understanding competitive adsorption behavior in complex aqueous environments, such as wastewater, where multiple ionic species coexist. Experiments were conducted using single-ion systems (containing only one type of metal ion) and binary systems (comprising Cd^{2+} in the presence of another competing ion), with all cations introduced at equal initial concentrations. Specifically, each test involved 0.06 g of CDAM added to 250 mL of an aqueous solution containing 20 mg L^{-1} of metal ions, at pH 5.5 and a contact time of 45 minutes. The results of these experiments are presented in Table 5.

The data indicate that CDAM strongly prefers cadmium ions, achieving a removal efficiency of 96.8% when no competing ions are present. However, introducing additional metal species in binary systems revealed varying degrees of interference in Cd^{2+} sorption. While some ions, such as Mg^{2+}, Fe^{3+}, Al^{3+}, Cr^{3+}, V^{5+}, Ca^{2+}, and Zr^{4+}, showed minimal impact, leading to only slight reductions in cadmium removal, other metals significantly affected performance. In particular, Cu^{2+}, Ni^{2+}, and Zn^{2+} demonstrated the most pronounced competitive interactions, decreasing Cd^{2+} adsorption to 86.7%, 88.4%, and 97.1%, respectively.

These more significant competitive effects likely stem from the physicochemical similarities of these ions to Cd^{2+}, particularly in ionic radius, charge density, and coordination chemistry. For example, Ni^{2+} and Cu^{2+} have comparable hydrated radii and a strong tendency to form stable complexes with functional groups such as amines and carboxyls, which are abundant on the surface of CDAM. Such competition suggests these ions may directly compete with Cd^{2+} for the same active sites on the sorbent surface.

This behavior underscores the importance of evaluating adsorbent selectivity in the presence of multiple coexisting ions, as is typical in real-world wastewater treatment scenarios.

Table 5 Effect of coexisting ions on Cd^{2+} ions uptake using CDAM sorbent in single and binary systems

Single system	Adsorption%	Binary system	Adsorption%
Cd^{2+}	96.8	Cd^{2+}	96.8
Mg^{2+}	1.0	Cd^{2+} + Mg^{2+}	96.6
Fe^{3+}	0.8	Cd^{2+} + Fe^{3+}	96.7
Al^{3+}	1.5	Cd^{2+} + Al^{3+}	96.3
Cr^{3+}	1.3	Cd^{2+} + Cr^{3+}	96.5
V^{5+}	1.1	Cd^{2+} + V^{5+}	96.1
Mn^{2+}	1.2	Cd^{2+} + M^{2+}	96.4
Ni^{2+}	13.6	Cd^{2+} + Ni^{2+}	88.4
Cu^{2+}	14.9	Cd^{2+} + Cu^{2+}	86.7
Pb^{2+}	3.5	Cd^{2+} + Pb^{2+}	93.2
Zn^{2+}	11.8	Cd^{2+} + Zn^{2+}	97.1
Zr^{4+}	0.5	Cd^{2+} + Zr^{4+}	96.3
Ca^{2+}	1.3	Cd^{2+} + Ca^{2+}	96.5

Although CDAM maintains a high selectivity for cadmium under most conditions, a reduction in performance has been observed. The presence of certain metals highlights potential challenges that could arise in practical applications. These findings emphasize the need for further optimization or functional modification to enhance the specificity of CDAM in environments where competitive adsorption from chemically similar ions may occur.

3.5. Mechanism of interaction between CDAM and Cd^{2+}

The adsorption of Cd^{2+} onto CDAM proceeds *via* a combined chelation–electrostatic mechanism in which the amine- and Schiff-base nitrogen atoms serve as primary coordination sites while the protonated amines ($-NH_3^+$) facilitate ion-exchange attraction. As Cd^{2+} ions approach the modified cellulose network, they are first drawn into proximity by electrostatic interactions with the positively charged quaternary ammonium and protonated secondary amine groups. Once localized at the surface, each Cd^{2+} ion forms coordinate bonds to available lone-pair donors—chiefly the imine (C=N) and primary/secondary amine (–NH–) nitrogens—creating stable five- or six-membered chelate rings. Hydroxyl oxygen atoms on the cellulose backbone may also contribute weaker coordination interactions, further stabilizing the bound metal. This multidentate binding motif concentrates Cd^{2+} at the adsorbent interface and secures it through strong covalent-like bonds, yielding the high uptake capacity and rapid kinetics observed (Scheme 2).

3.6. Desorption and durability studies

The capability to regenerate adsorbent materials is crucial for their large-scale use, environmental sustainability, and cost-effectiveness. A comprehensive desorption study was conducted using various chemical agents to assess the reusability of the CDAM. These included (HCl), (H_2SO_4), (HNO_3), ethylenediaminetetraacetic acid (EDTA), and Acetic acid (CH_3COOH). Each agent was evaluated at a concentration of 1 M under uniform conditions—15 minutes of contact time at 25 °C—after which it was thoroughly rinsed using ionized water before reapplication of the adsorbent.

Among the tested eluents, hydrochloric acid (HCl) demonstrated the most effective desorption performance for Cd^{+2} recovery from CDAM, as evidenced by the comparative data shown in Fig. 12A. The elution efficiency of HCl was further

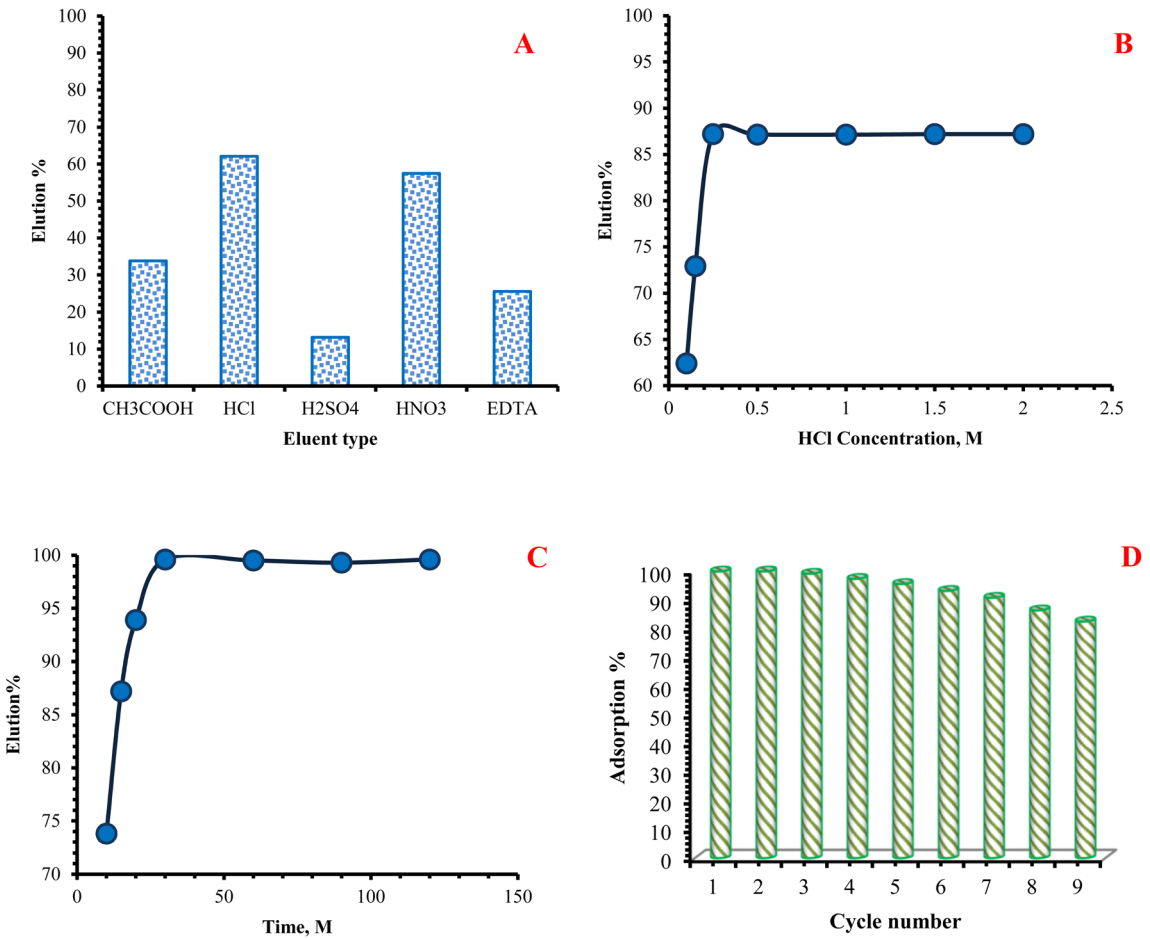

Fig. 12 (A) Effect of different eluting agents, (B) effect of HCl concentration, (C) effect of time on the desorption of cadmium from CDAM, and (D) recycling ability of CDAM for Cd^{2+} in consecutive nine cycles.

optimized by investigating its concentration range from 0.1 M to 2 M while maintaining constant desorption parameters. The results, depicted in Fig. 12B, indicate that 0.25 M HCl achieves the highest cadmium desorption efficiency, suggesting that higher acid concentrations do not necessarily enhance recovery and may instead compromise the adsorbent's structural integrity or functional activity.

Additionally, the influence of the desorption contact period was systematically considered over 30 to 180 minutes to determine the optimal recovery period. As illustrated in Fig. 12C, the Cd^{+2} recovery increased steadily with time and reached near-complete desorption at 30 minutes, beyond which no significant improvement was observed. These findings establish that a 30-minute desorption cycle using 0.25 M HCl at room temperature provides optimal conditions for effective regeneration of the CDAM adsorbent. In contrast, the CDAM material developed in this study demonstrated considerable ease in adsorption and regeneration operations. As shown in Fig. 12D, the batch reusability tests revealed that CDOP maintained nearly constant removal efficiency over the first 9 consecutive cycles. A slight decline to 82.4% was observed after the eighth cycle, which can be attributed to incomplete desorption or residual Cd^{2+} on the adsorbent surface.

3.7. Application in real samples

The working sample was collected from the Wadi Um-Gheig region. Two characteristic ore samples and two waste samples were obtained from the Um-Gheig area. The rock samples were crushed to pass through a 60-mesh sieve and thoroughly rinsed with excess tap water to remove slimes. The cleaned samples were then permitted to dry. A portion of the ore (1 g) was further ground to pass through a 200-mesh sieve and thoroughly digested using an appropriate acid mixture. The chemical characteristics of the sample are presented in Table 6.

It is important to mention herein that, in the Cd(II) sorption method from the samples S1 and S2, we observed a serious problem with the concentration of Zn^{2+} content, which is a serious problem in the adsorption process of Cd^{2+}. Therefore, this content must be removed through a separation process, which can be summarized as follows: next to leaching with 40% H_2SO_4, the separation of zinc occurred using ammonium hydroxide by adjusting the pH to 8.5, after that CO_2 gas was flowed through the leach liquor solution with stirring tell the Zinc precipitation was formed.[78] The obtained zinc carbonate was converted to zinc oxide through thermal decomposition at 350 °C, which was sufficient for the complete decomposition of zinc carbonate for three hours. The obtained zinc oxide was confirmed using different tools, XRD and SEM.

Fig. 13 shows the XRD pattern of ZnO in nanoparticle form, recorded over a 2θ range of 10° to 80°. The presence of distinct peaks in the pattern confirms that the ZnO nanoparticles are semi-crystalline. The observed diffraction peaks at 2θ values of 31.9°, 34.56°, 36.42°, 47.62°, 56.8°, 63.04°, and 68.14° correspond to the characteristic planes of the wurtzite structure of ZnO, as referenced by the JCPDS data card No. 36–1451. These data are consistent with previously reported XRD patterns for ZnO nanoparticles.[79,80]

Energy-dispersive X-ray (EDX) analysis confirmed the high purity of the ZnO nanoparticles, with the elemental composition consisting primarily of zinc and oxygen. Scanning electron microscopy (SEM) images revealed a flaky morphology, characterized by flat and irregularly shaped nanocrystalline flakes.

500 mL of each sample were subjected to adsorption process using CDAM adsorbent using the best controlling factors reached (pH 5.5, 1.5 g CDAM dose, 45 min time at 70 °C) after that the pregnant CDAM with Cd^{2+} were separated and the Cd^{2+} was eluted using 0.25 M HCl for 30 min, finally the CDAM was separated and washed several time to be ready to used again.

The recovered cadmium solution was subjected to precipitation as a flow. First, the pH was adjusted to 8–9 using NH_4OH solution added dropwise with continuous stirring to form $Cd(OH)_2$ precipitate. After stirring for 30 minutes, allow the precipitate to settle for two to three hours, then filter using vacuum filtration with Whatman filter paper and wash thoroughly with deionized water until chloride-free (test with $AgNO_3$). Dry the precipitate at 80–100 °C for 4–6 hours. The obtained

Table 6 Chemical composition of Wadi Um-Gheig rock sample (S1 and S2), chemical composition of Wadi Um-Gheig waste sample (S3 and S4)

	Concentration, (%)		Concentration (ppm)	
Element	S1	S2	S1	S2
SiO_2	3.1	4.34	1100	1877
Al_2O_3	1.3	0.86	27	44
CaO	28.4	8.01	240	180
MgO	4.2	0.56	390	416
Fe_2O_3	12.1	4.07	23	16
Na_2O	0.38	0.36	81	93
K_2O	0.17	0.13	24	33
ZnO	20.1	37.5	39	51
MnO	0.55	0.38	34	28
PbO	2.5	1.55	417	439
L.O.I	25.8	29.33		

Sample	pH	Ca^{2+}	Mg^{2+}	Na^{+}	K^{+}	Cl^{-}	CO_3^{2-}	SO_4^{2-}	Th^{4+}	UO^{2+}	Cd^{2+}	Pb^{2+}
S3	3	2548	1035	34 812	1567	36 313	2045	2322	31	33.6	196.5	15.4
S4	3.8	3381	2001	35 794	1318	36 424	2793	2938	461	21.5	101.3	22.3

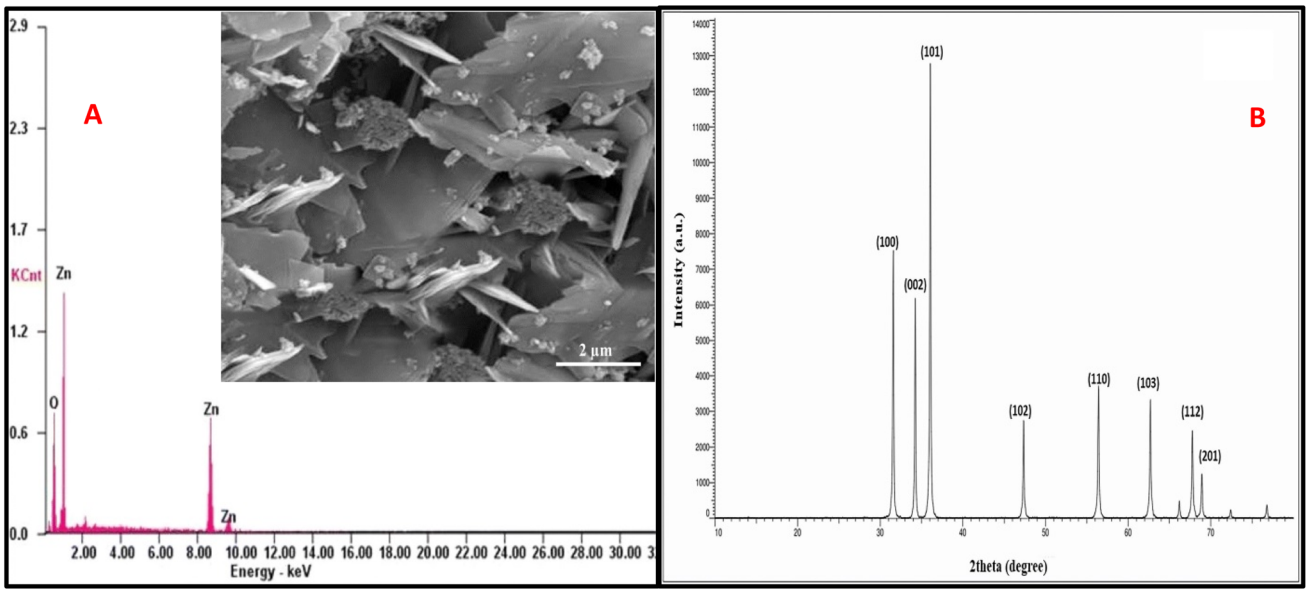

Fig. 13 (A) EDX, SEM, and (B) XRD analysis of produced ZnO.

precipitate is divided into two portions: one is converted directly to CdO product, and the other is converted to cadmium nanoparticles. The first portions are transferred to a ceramic crucible and calcined in a muffle furnace at 300–350 °C for 120–180 min. to convert them to CdO according to the reaction eqn (14):

$$Cd(OH)_2 \rightarrow CdO + H_2O \quad (14)$$

The resulting brown to red-brown CdO powder should be cooled in a desiccator and kept in an airtight container. The obtained product was confirmed using XRD analysis and SEM.

Subsequently, cadmium sorption was carried out using CDAM under optimized conditions: pH 5.5, 0.06 g of CDAM, 45 min. of reaction period, and a temperature of 70 °C. The Cd(II)-loaded CDAM was then eluted using 0.25 M HCl. Finally, cadmium was precipitated using Na_2S, and the resulting product was investigated by X-ray diffraction (XRD) analysis (Fig. 14).

The XRD pattern (Fig. 14) confirms the formation of the CdO phase with a lattice constant of 4.695 Å and a cubic crystal structure belonging to the space group Fm3m. The diffraction peaks observed at 2θ values of 32.90°, 38.20°, 55.20°, 65.80°, and 69.20° correspond to the (111), (200), (220), (311), and (222) planes, respectively, which match the standard pattern for cubic CdO (JCPDS card No. 05-0640). These results indicate the successful synthesis of crystalline CdO.

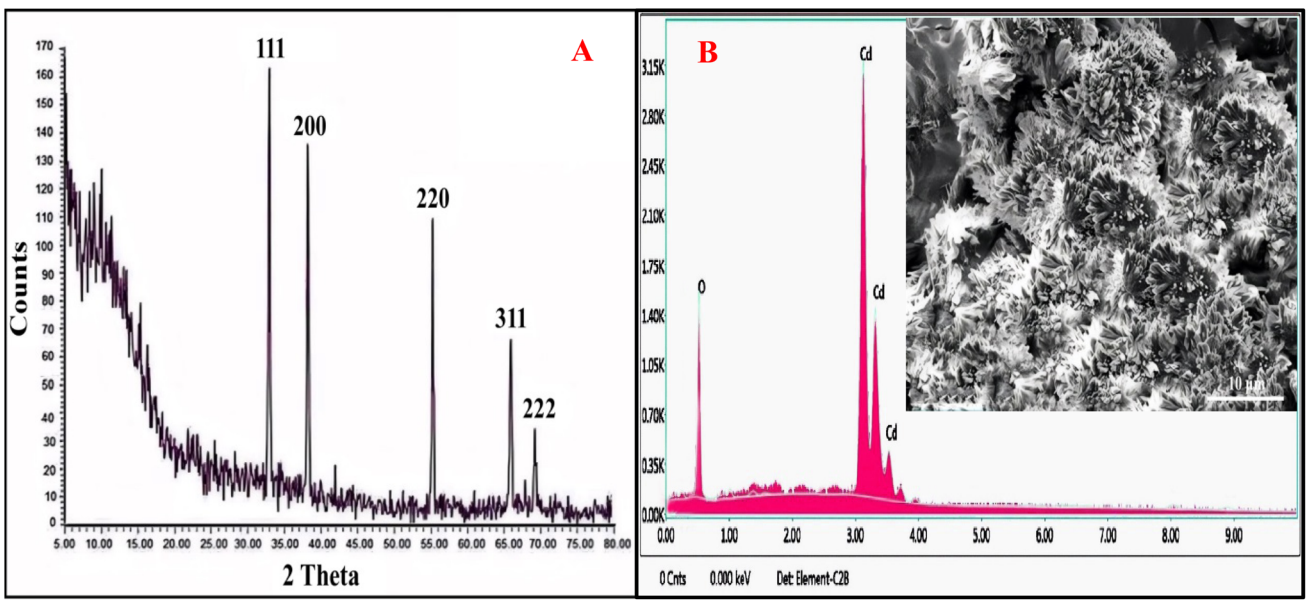

Fig. 14 (A) XRD, and (B) EDX, SEM, analysis of the produced CdO.

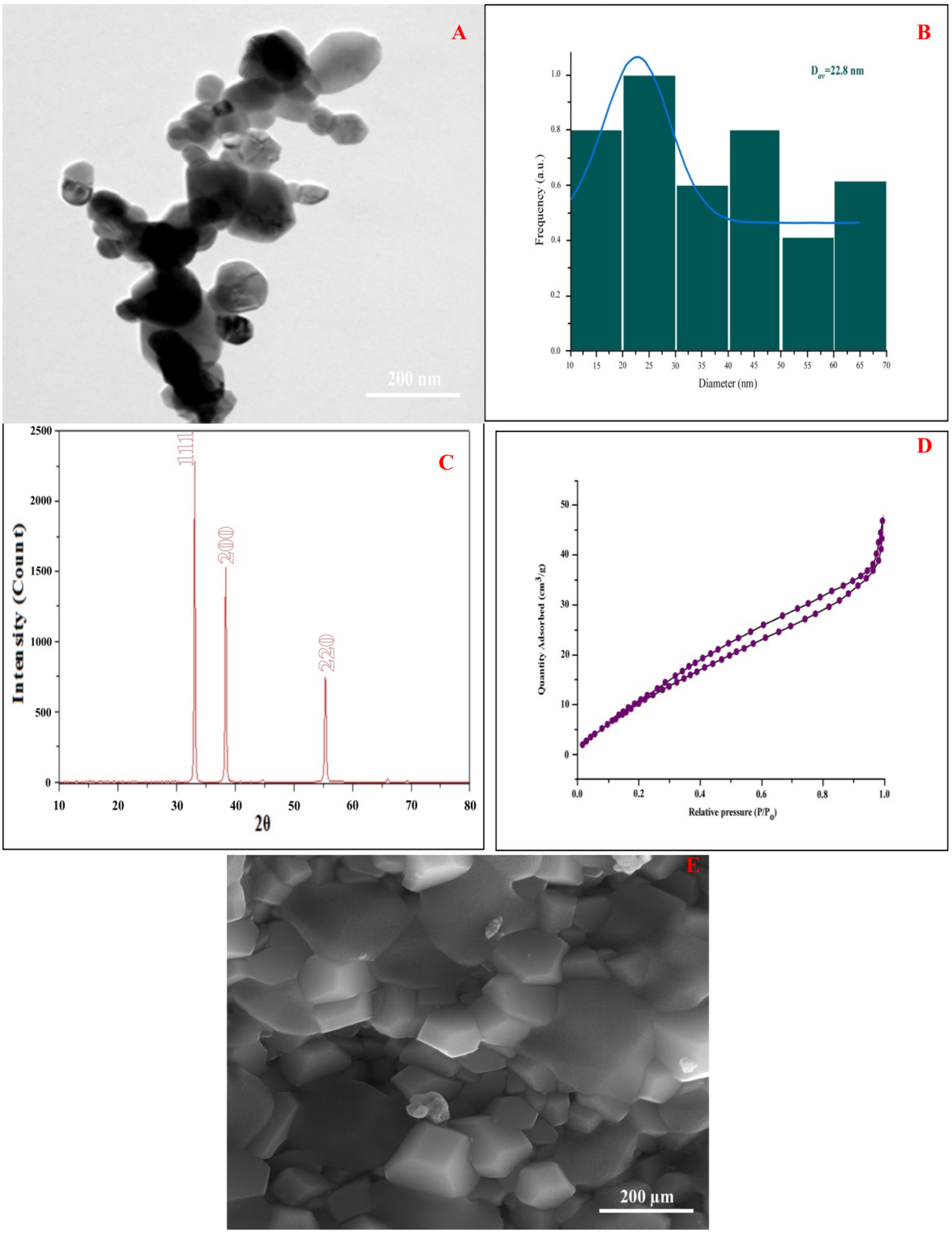

Fig. 15 (A) high-resolution transmission electron microscopy image, (B) average particle size (C) XRD analysis, (D)BET analysis, (E) SEM image, of CdO nanoparticles.

SEM images of the CdO sample reveal a distinctive cauliflower-like morphology, characterized by clustered and aggregated nanostructures.

The 2nd portion was then used to preparation of cadmium nano particle as follow, The obtained cadmium hydroxide was converted to cadmium nitrate, thoroughly wash the $Cd(OH)_2$ precipitate with deionized water 3–4 times and filter using vacuum filtration with Whatman filter paper, then place the washed precipitate in a clean beaker and add 2 M HNO_3 dropwise with continuous stirring until complete dissolution occurs according to the reaction, eqn (15):

$$Cd(OH)_2 + 2HNO_3 \rightarrow Cd(NO_3)_2 + 2H_2O \quad (15)$$

Using minimal acid for dissolution, filter the resulting solution *via* a 0.45 μm membrane filter to eliminate any undissolved particles. Then, heat the filtrate on a hot plate at 70–80 °C with stable stirring to evaporate excess water, obtaining a concentrated $Cd(NO_3)_2$ solution. Avoid complete drying. Finally, the solution should be allowed to cool to room temperature before further processing.[81,82]

To synthesize CdO nanoparticles, dissolve 0.12 M of the prepared cadmium nitrate tetrahydrate ($Cd(NO_3)_2$) in 150 mL of deionized water in a 250 mL flask with continuous stirring. Adjust the pH to 11 by adding 25% w/w ammonia solution dropwise, which causes the formation of cadmium hydroxide intermediate, and stir the solution for 12 hours to ensure complete reaction. Transfer the mixture to a 250 mL autoclave and heat at 80 °C for 12 hours for hydrothermal treatment, promoting controlled nucleation and uniform nanostructure growth. Collect the white precipitate (cadmium hydroxide precursor) by centrifugation, wash several times with distilled water to remove residual ions, and dry overnight at 60 °C. Finally, calcine the dried material at 600 °C for 3 hours in a furnace to convert the hydroxide precursor to brown CdO nanoparticles through thermal decomposition, yielding crystalline nanoparticles with controlled size distribution and high purity suitable for various applications in catalysis, sensing, and electronic devices.

The high-resolution transmission electron microscopy image (Fig. 15a) of CdO nanoparticles reveals particles with a predominantly cubic morphology. The presence of larger particles is attributed to the aggregation of smaller particles. A log-normal fit of the particle size distribution attained from the TEM image yielded an average particle diameter of approximately 22.7 nm. The corresponding histogram and average particle size are presented in Fig. 15b. This average particle size is consistent with that calculated from X-ray diffraction (XRD) data.

Fig. 15 displays the powder XRD pattern of CdO nanoparticles, indicating a cubic crystal structure with unit cell parameters: $a = b = c = 4.694$ Å and $\alpha = \beta = \gamma = 90°$. The average particle size, estimated using Scherrer's equation, was approximately 31 nm. The sharp and well-defined diffraction peaks confirm the crystalline nature of the CdO nanoparticles with random orientation.[83] The diffraction peaks corresponding to the (111), (200), and (220) planes align well with the standard JCPDS card No. 75-0593, confirming the phase purity of CdO.

The surface area and pore structure of the CdO nanoparticles were evaluated by nitrogen physisorption analysis. The nitrogen adsorption–desorption isotherms (Fig. 15b) correspond to a type IV isotherm with an H3 hysteresis loop, as classified by IUPAC.[84] This type of hysteresis suggests the presence of slit-like mesopores, consistent with the mesoporous nature of the CdO particles (Gregg & Sing, 1982). The Brunauer–Emmett–Teller (BET) surface area was measured at 58.4 $m^2\ g^{-1}$, with a total pore volume of 0.059 $cm^3\ g^{-1}$. The Barrett–Joyner–Halenda (BJH) desorption pore size distribution revealed an average pore size of 4.7 nm, confirming the mesoporous structure and indicating high surface contact potential.

The shape and morphology of the CdO nanoparticles were further examined using FE-SEM. As shown in Fig. 15, the CdO nanoparticles exhibit a polygonal structure with an almost uniform size distribution.

The synthesis of high-purity CdO nanoparticles from recovered waste streams demonstrates a successful transition from environmental pollutant to functional nanomaterial. The produced CdO, with its crystalline structure and morphology, is not a waste product but a valuable material with several potential applications. CdO nanoparticles are known for their use in optical devices due to their transparent conductivity and high carrier mobility, in gas sensors for their sensitivity to various gases, as a photocatalyst for the degradation of organic pollutants, and as an electrode material in batteries and solar cells.[74,75] This valorization pathway significantly enhances the economic feasibility and environmental benefits of the adsorption process, aligning perfectly with the principles of a circular economy.

4. Conclusion

This work demonstrated the design, synthesis, and performance of a novel amine-functionalized, Schiff-base grafted cellulose network (CDAM) for highly efficient Cd^{2+} removal and subsequent value-added nanoparticle synthesis. Comprehensive spectroscopic and thermal analyses (FTIR, XPS, $^1H/^{13}C$-NMR, GC-MS, TGA) confirmed successful covalent attachment of multi-amine sites onto the cellulose backbone, endowing CDAM with abundant nitrogen-donor ligands and enhanced structural stability. Under optimized conditions (pH 5.5, 30 min contact, 0.06 g L^{-1} dose, 298 K), CDAM achieved an unprecedented Cd^{2+} uptake capacity of 483.7 mg g^{-1}, far exceeding most reported biosorbents. Kinetic modeling revealed a pseudo-second-order mechanism ($R^2 > 0.99$), indicating chemisorption through Cd–N/O coordination. At the same time, equilibrium data fit the Langmuir isotherm ($q_m \approx 476$ mg g^{-1}, $R^2 = 0.993$), supporting monolayer coverage on a homogeneous surface. The thermodynamic study confirmed that adsorption is endothermic, spontaneous, and driven by increased randomness at the interface. High-resolution XPS of Cd-loaded CDAM directly evidenced Cd–N coordination (Cd $3d_{5/2}$ at 405.1 eV, $3d_{3/2}$ at 411.9 eV alongside shifted N 1s peaks). CDAM proved highly reusable, retaining over 90% of its initial capacity after

seven uptake and elution cycles with 0.25 M HCl. In a real-world scenario, CDAM quantitatively recovered Cd^{2+} from acid leachates of Wadi Um-Gheig rock samples, and the eluate was converted to crystalline CdO nanoparticles (monoclinic phase, surface area = 58.4 m^2 g^{-1}) *via* controlled precipitation and calcination. Collectively, these results establish CDAM as a highly effective, sustainable platform for cadmium remediation and resource recovery, with significant implications for industrial wastewater treatment and circular-economy valorization of heavy-metal waste streams. Collectively, these results establish CDAM not merely as an adsorbent, but as a highly effective and sustainable platform that integrates two value-adding processes: efficient cadmium remediation and resource recovery. This dual-purpose strategy, which combines environmental purification with the simultaneous synthesis of value-added nanoparticles, presents significant implications for industrial wastewater treatment and circular economy strategies.

Conflicts of interest

The authors declare no conflict of interest.

Data availability

The data that support the findings of this study are available from the corresponding author upon reasonable request.

Acknowledgements

The authors extend their appreciation to the Deputyship for Research & Innovation, Ministry of Education in Saudi Arabia for funding this research work through the project number MoE-IF-UJ- R2-22- 1644-2.

References

1 J. Sun, F. Lian, Z. Liu, L. Zhu and Z. Song, Biochars derived from various crop straws: characterization and Cd(II) removal potential, *Ecotoxicol. Environ. Saf.*, 2014, **106**, 226–231.

2 T. Huang, L. Hu, J. Wu, W. Zhang and L. Mao, Characteristics of bovine bone biochar at different pyrolysis temperatures and its adsorption of Cd^{2+}, *J. Agro-Environ. Sci.*, 2023, **42**, 1632–1644.

3 L. Zhao, M. Liao, L. Li, L. Chen, T. Zhang and R. Li, Cadmium activates the innate immune system through the AIM2 inflammasome, *Chem.-Biol. Interact.*, 2024, **399**, 111122.

4 J. Luo and S. Lin, Association between cadmium exposure and serum neurofilament light chain levels: a nationwide population-based survey, *Ecotoxicol. Environ. Saf.*, 2024, **282**, 116771.

5 H. Wang, C. Jin, X. Li, J. Ma, Y. Ye, L. Tang, *et al.*, A green biocatalyst fabricated by fungal laccase immobilized onto Fe_3O_4@polyaniline-chitosan nanofibrous composites for the removal of phenolic compounds, *Chem. Eng. J.*, 2025, **507**, 160486.

6 M. Khairy, S. A. El-Safty and M. A. Shenashen, Environmental remediation and monitoring of cadmium, *TrAC, Trends Anal. Chem.*, 2014, **62**, 56–68.

7 X. Cui, S. Fang, Y. Yao, T. Li, Q. Ni, X. Yang, *et al.*, Potential mechanisms of cadmium removal from aqueous solution by *Canna indica* derived biochar, *Sci. Total Environ.*, 2016, **562**, 517–525.

8 B. G. Fouda-Mbanga, E. Prabakaran and K. Pillay, Carbohydrate biopolymers, lignin-based adsorbents for removal of heavy metals (Cd^{2+}, Pb^{2+}, Zn^{2+}) from wastewater, regeneration and reuse for spent adsorbents including latent fingerprint detection: a review, *Biotechnol. Rep.*, 2021, **30**, e00609.

9 Z. Cui, K. Yang, Y. Shen, Z. Yuan, Y. Dong, P. Yuan, *et al.*, Toxic gas molecules adsorbed on intrinsic and defective WS2: gas sensing and detection, *Appl. Surf. Sci.*, 2023, **613**, 155978.

10 L. Luan, B. Tang, Y. Liu, W. Xu, Y. Liu, A. Wang, *et al.*, Direct synthesis of sulfur-decorating PAMAM dendrimer/mesoporous silica for enhanced Hg(II) and Cd(II) Adsorption, *Langmuir*, 2022, **38**, 698–710.

11 K. Wu, B. Wang, B. Tang, L. Luan, W. Xu, B. Zhang, *et al.*, Adsorption of aqueous Cu(II) and Ag(I) by silica anchored Schiff base decorated polyamidoamine dendrimers: behavior and mechanism, *Chin. Chem. Lett.*, 2022, **33**, 2721–2725.

12 W. Qiao, P. Zhang, L. Sun, S. Ma, W. Xu, S. Xu, *et al.*, Adsorption performance and mechanism of Schiff base functionalized polyamidoamine dendrimer/silica for aqueous Mn(II) and Co(II), *Chin. Chem. Lett.*, 2020, **31**, 2742–2746.

13 A. Wang, S. Li, H. Chen, Y. Hu and X. Peng, Synthesis and characterization of a novel microcrystalline cellulose-based polymeric bio-sorbent and its adsorption performance for Zn(II), *Cellulose*, 2019, **26**, 6849–6859.

14 Y. Xiao, X. Zhu, H. Zheng, Q. Tang and R. Qiu, Preparation of phosphorylated rice husk for cadmium adsorption: crucial role of phosphoryl group, *Bioresour. Technol.*, 2024, **408**, 131159.

15 M. Marszałek, E. Knapik, M. Piotrowski and K. Chruszcz-Lipska, Removal of cadmium from phosphoric acid in the presence of chloride ions using commercially available anion exchange resins, *J. Ind. Eng. Chem.*, 2023, **118**, 488–498.

16 W. Huang, Z. Chen, H. Liu, H. Wang and Z. Wei, Microbial induced carbonate precipitation for cadmium removal in flue gas from sludge incineration, *J. Environ. Chem. Eng.*, 2024, **12**, 112573.

17 P. Wanichapichart, W. Bootluck, P. Thopan and L. D. Yu, Influence of nitrogen ion implantation on filtration of fluoride and cadmium using polysulfone/chitosan blend membranes, *Nucl. Instrum. Methods Phys. Res., Sect. B*, 2014, **326**, 195–199.

18 K. Geng, J. Jin, J. Chai and Y. Qin, Adsorption characteristics and mechanism analysis of heavy metal Zn^{2+} by cement-soil and alkali activated slag-bentonite-soil, *Case Stud. Constr. Mater.*, 2024, **21**, e03583.

19 K. Dou, W. Zhao, C. Wang, Y. Fan, C. He, L. Zhang, *et al.*, Switch on amine substrate reactivity towards hexaazaisowurtzitane cage: Insights from a tailored machine learning model, *Chem. Eng. J.*, 2024, **501**, 157677.
20 S. Gomez-Salazar, J. S. Lee, J. C. Heydweiller and L. L. Tavlarides, Analysis of Cadmium Adsorption on Novel Organo-Ceramic Adsorbents with a Thiol Functionality, *Ind. Eng. Chem. Res.*, 2003, **42**(14), 3403–3412.
21 M. Garoub and M. Gado, Separation of Cadmium Using a new Adsorbent of Modified Chitosan with Pyridine Dicarboxyamide derivative and application in different samples, *Z. fur Anorg. Allg. Chem.*, 2021, **648**, 28–47.
22 H. A. Ibrahium, B. M. Atia, N. S. Awwad, A. A. Nayl, H. A. Radwan and M. A. Gado, Efficient preparation of phosphazene chitosan derivatives and its applications for the adsorption of molybdenum from spent hydrodesulfurization catalyst, *J. Dispersion Sci. Technol.*, 2022, 2103–2118.
23 E. Guibal, Interactions of metal ions with chitosan-based sorbents: a review, *Sep. Purif. Technol.*, 2004, **38**(1), 43–74.
24 H. Shameem, K. Abburi, G. K. Tushar, V. S. Dabir, B. M. Veera and S. D. Edgar, Adsorption of Divalent Cadmium (Cd(II)) from Aqueous Solutions onto Chitosan-Coated Perlite Beads, *Ind. Eng. Chem. Res.*, 2006, **45**(14), 5066–5077.
25 X. Zhang, H. Liu, J. Yang, L. Zhang, B. Cao, L. Liu, *et al.*, Reviews on, *Adv. Mater.*, 2021, **60**, 365–376.
26 H. A. Ibrahium, N. S. Awwad, M. A. Gado, M. A. Hassanin, A. A. Nayl and B. M. Atia, Physico-chemical aspects on uranium and molybdenum extraction from aqueous solution by synthesized phosphinimine derivative chelating agent, *J. Inorg. Organomet. Polym. Mater.*, 2022, **32**, 3640–3657.
27 Y. Cai, J. Li, Q. Zhang, C. Liu, C. Wang, H. Shi, *et al.*, Ambient ultrafast green synthesis of cyclodextrin-based metal–organic framework through solvent-induced in-situ crystallization for high-efficiency capture of radioactive iodine, *Sep. Purif. Technol.*, 2025, **376**, 134078.
28 T. Suopajarvi, H. Liimatainen, O. Hormi and K. J. Niinima, Coagulation flocculation treatment of municipal wastewater based on anionized nanocelluloses, *Chem. Eng. J.*, 2013, **231**, 59–67.
29 J. Lu, X. Han, L. Dai, C. Li, J. Wang, Y. Zhong, *et al.*, Conductive cellulose nanofibrils-reinforced hydrogels with synergetic strength, toughness, selfadhesion, flexibility and adjustable strain responsiveness, *Carbohydr. Polym.*, 2020, **250**, 117010.
30 X. Gong, Z. Cheng, S. Gao, D. Zhang, Y. Ma, J. Wang, *et al.*, Ethyl cellulose based self-healing adhesives synthesized *via* RAFT and aromatic schiff-base chemistry, *Carbohydr. Polym.*, 2020, **250**, 116846.
31 G. Lin, S. Wang, L. Zhang, T. Hu, J. Peng, S. Cheng, *et al.*, Synthesis and evaluation of thiosemicarbazide functionalized corn bract for selective and efficient adsorption of Au(III) from aqueous solutions, *J. Mol. Liq.*, 2018, **258**, 235–243.
32 F. Liu, G. Peng, T. Li, G. Yu and S. Deng, Au(III) adsorption and reduction to gold particles on cost-effective tannic acid immobilized dialdehyde corn starch, *Chem. Eng. J.*, 2019, **370**, 228–236.
33 S. A. Mahmoud, B. M. Atia and M. Abdalla, Polyvinyl alcohol-conjugated L-cysteine: a novel metal pincer for efficient heavy metal ions removal from wastewater, *ChemistrySelect*, 2024, **9**, e202401169.
34 M. Mohery, G. M. Mahran, B. M. Atia and M. A. Gado, Removal of lead ions from wastewater by a new chelating amidoxime based-mesoporous silica, *Inorg. Chem. Commun.*, 2025, **180**, 114884.
35 Z. Dong, X. Yang, Q. Pan, Y. Ao, J. Du, M. Zhai, *et al.*, Performance and mechanism of selective adsorption of silver to L-cysteine functionalized cellulose microsphere, *Cellulose*, 2020, **27**, 3249–3261.
36 S. A. Mahmoud, L. G. Amin, B. M. Atia and M. Gado, Sustainable recovery of silver from X-ray film processing effluents using a novel thiourea derivative-grafted XAD-7 resin and its application in nano silver particle synthesis, *Int. J. Environ. Anal. Chem.*, 2025, DOI: **10.1080/03067319.2025.2505934**.
37 A. A. Weshahy, A. A. Gouda, R. E. Shohaib, B. M. Atia and M. A. Gado, Adsorption and recovery of neodymium and praseodymium from magnet waste NdFeB using a novel pyridine Schiff base compound, *ChemistrySelect*, 2025, **10**, e202404297.
38 J. Zhang, C. Ma, Q. Xia, J. Liu, Z. Ding, M. Xu, *et al.*, Composite electrolyte membranes incorporating viscous copolymers with cellulose for high-performance lithium-ion batteries, *J. Membr. Sci.*, 2016, **497**, 259–269.
39 L. Zheng, Z. Dang, C. Zhu, X. Yi, H. Zhang and C. Liu, Removal of cadmium(II) from aqueous solution by corn stalk graft copolymers, *Bioresour. Technol.*, 2010, **101**, 5820–5826.
40 X. Xu, M. Wang, Q. Wu, Z. Xu and X. Tian, Synthesis and Application of Novel Magnetic Ion-Imprinted Polymers for Selective Solid Phase Extraction of Cadmium(II), *Polymers*, 2017, **9**, 360.
41 O. P. Tkachenko, E. S. Shpiro, M. Wark, G. Schulz-Ekloff and N. I. Jaeger, X-ray photoelectron/X-ray excited auger electron spectroscopic study of highly dispersed semiconductor CdS and CdO species in zeolites, *J Chem Soc Faraday Trans*, 1993, **89**, 3987–39872394; A. R. Weshahy, A. A. Gouda, B. M. Atia, A. K. Sakr, J. S. Al-Otaibi, A. Almuqrin, *et al.*, Efficient recovery of rare earth elements and zinc from spent Ni–metal hydride batteries: statistical studies, *Nanomaterials*, 2022, **12**, 2305.
42 S. Zhuang, Q. Zhang and J. Wang, Adsorption of Co^{2+} and Sr^{2+} from aqueous solution by chitosan grafted with EDTA, *J. Mol. Liq.*, 2021, **325**, 115197.
43 M. A. Gado, Efficient adsorption of thorium and cerium from Rosetta monazite concentrate using a novel phosphorylated Schiff-base adsorbent, *J. Radioanal. Nucl. Chem.*, 2024, 5025–5048.
44 M. Abdalla, Adsorption of vanadium using a new anionic Schiff base adsorbent and its application to vanadium

separation from boiler ash, *J. Chem. Technol. Biotechnol.*, 2024, DOI: 10.1002/jctb.7733.

45 M. A. Hendy, T. I. Kashar, E. M. Allam, M. A. Gado, N. S. Yahia and M. F. Cheira, Synthesis of pyridine dicarboxylic acid functionalized and crosslinked to polyvinyl alcohol/polyamide for thorium capturing from aqueous solution, *ChemistrySelect*, 2024, **9**, e202402329.

46 N. S. Awwad, H. M. Younis, H. A. Ibrahium, B. M. Atia and M. A. Gado, Efficient and sustainable design of pyridyl-bis-thiourea pincer ligand-immobilised Merrifield polymer precursor for arsenic ions adsorption, *Int. J. Environ. Anal. Chem.*, 2024, 1–32.

47 J. Liang, X. Li, Z. Yu, G. Zeng, Y. Luo, L. Jiang, *et al.*, Amorphous MnO2 modified biochar derived from aerobically composted swine manure for adsorption of Pb(II) and Cd(II), *ACS Sustain. Chem. Eng.*, 2017, **5**, 5049–5058.

48 M. A. Bajaber, A. H. Ragab, A. K. Sakr, B. M. Atia, W. M. Fathy and M. A. Gado, Application of new derivatives of triazole Schiff base on chromium recovery from its wastewater, *Sep. Sci. Technol.*, 2023, **58**, 737–758.

49 A. A. Alluhaybi, A. Alharbi, A. M. Hameed, A. A. Gouda, F. S. Hassen, H. S. El-Gendy, *et al.*, A novel triazole Schiff base derivatives for remediation of chromium contamination from tannery wastewater, *Molecules*, 2022, **27**, 5087.

50 S. A. Mahmoud, B. M. Atia, L. G. Amin and M. Abdalla, Innovative preparation of multi-dentate Schiff base adsorbent for the adsorption of silver and its application on nano silver particles preparation from liquid photographic wastes, *J. Chem. Technol. Biotechnol.*, 2024, 448–465.

51 B. M. Atia, H. A. Radwan, W. A. Kassab, H. K. Sarhan, M. A. Gado and A. E. Goda, Highly efficient recovery of vanadium from Abu Zeneima ferruginous siltstone, Southwestern Sinai, Egypt, by a novel polyimine-based chelating ligand, *J. Chin. Chem. Soc.*, 2024, **71**, 507–520.

52 I. Langmuir, The constitution and fundamental properties of solids and liquids, *J. Am. Chem. Soc.*, 1916, **38**, 2221–2295.

53 R. E. Elbshary, A. A. Gouda, R. E. Sheikh, M. S. Alqahtani, M. Y. Hanfi, B. M. Atia, *et al.*, Recovery of W(VI) from wolframite ore using new synthetic Schiff base derivative, *Int. J. Mol. Sci.*, 2023, **24**, 7423.

54 B. M. Atia, M. F. Cheira, M. A. Hassanin, H. S. El-Gendy, M. E. Elawady, H. K. Sarhan, *et al.*, Enhanced boron recovery by a new synthesized polyvinyl alcohol anchored gallic acid moiety *via* ethyl carbamate linker, *Sep. Sci. Technol.*, 2023, 2307–2330.

55 H. M. F. Freundlich, Uber die adsorption in lösungen, *Z. Phys. Chem.*, 1906, **57A**, 385–470.

56 M. Temkin and V. Pyzhev, Kinetics of ammonia synthesis on promoted iron catalysts, *Acta Physicochim. URSS*, 1940, **12**, 217–222.

57 A. Ene, H. M. H. Zakaly, A. R. Salem, A. A. Gouda, K. Althumayri, K. F. Alshammari, *et al.*, A new partially phosphorylated polyvinyl phosphate-PPVP composite: Synthesis and its potentiality for Zr(IV) extraction from an acidic medium, *Separations*, 2022, **9**, 382.

58 M. M. Dubinin and L. V. Radushkevich, Equation of the characteristic curve of activated charcoal, *Chem. Zentralbl.*, 1947, **1**, 875–890.

59 M. Polanyi, Theories of the adsorption of gases. A general survey and some additional remarks. Introductory paper to section III, *Trans. Faraday Soc.*, 1932, **28**, 316–333.

60 A. R. Weshahy, A. K. Sakr, A. A. Gouda, B. M. Atia, H. H. Somaily, M. Y. Hanfi, *et al.*, Selective recovery of cadmium, cobalt, and nickel from spent Ni–Cd batteries using Adogen® 464 and mesoporous silica derivatives, *Int. J. Mol. Sci.*, 2022, **23**, 8677.

61 H. A. Ibrahium, A. M. M. Abdel, N. S. Awwad, B. M. Atia, H. E. Ali, M. A. Gado, *et al.*, Solid–liquid separation of V(V) from aqueous medium by 3-(2-hydroxy phenyl)-imino-1-phenyl butan-1-one Schiff base immobilized XAD-2 resin, *Int. J. Environ. Sci. Technol.*, 2022, 7689–7706.

62 A. M. Amin, H. A. Ibrahium, A. A. Gouda, R. E. Sheikh, B. M. Atia, M. A. Gado, *et al.*, Design and utilisation of a novel poly imino-phosphorane composite for the effective removal of Pb^{2+} and Cr^{3+} ions from contaminated water sources, *Int. J. Environ. Anal. Chem.*, 2024, 1–28.

63 S. A. Mahmoud, B. M. Atia and M. A. Gado, Efficient removal of toxic metals (Hg(II), Cr(II), Pb(II), Cd(II)) using high-performance polyvinyl alcohol-L-2-amino-3-mercaptopropionic acid composite from wastewater, *Int. J. Environ. Sci. Technol.*, 2025, 12269–12294.

64 M. A. Hendy, T. I. Kashar, E. M. Allam, M. A. Gado, N. S. Yahia and M. F. Cheira, Thorium ions elimination from its solution utilizing the assembled sulfosuccinic acid/polyvinyl alcohol/polyamide, *Mater. Today Commun.*, 2024, **40**, 109633.

65 A. Y. Li, T. Lu, Y. T. Zhang, S. J. Deng, X. J. Duan and G. H. Qiu, Mechanisms for synergistically enhancing cadmium remediation performance of biochar: silicon activation and functional group effects, *Bioresour. Technol.*, 2024, **404**, 130913.

66 A. Y. Li, C. H. Ye, Y. H. Jiang and H. Deng, Enhanced removal performance of magnesium-modified biochar for cadmium in wastewaters: role of active functional groups, processes, and mechanisms, *Bioresour. Technol.*, 2023, **386**, 129515.

67 X. Cui, S. Fang, Y. Yao, T. Li, Q. Ni, X. Yang, *et al.*, Potential mechanisms of cadmium removal from aqueous solution by Canna indica derived biochar, *Sci. Total Environ.*, 2016, **562**, 517–525.

68 C. B. Godiya, X. Cheng, D. Li, Z. Chen and X. Lu, Carboxymethyl cellulose/polyacrylamide composite hydrogel for cascaded treatment/reuse of heavy metal ions in wastewater, *J. Hazard. Mater.*, 2019, **364**, 28–38.

69 A. I. Ivanets, V. Srivastava, N. V. Kitikova, I. L. Shashkova and a M. Sillanpä, Non-apatite Ca-Mg phosphate sorbent for removal of toxic metal ions from aqueous solutions, *J. Environ. Chem. Eng.*, 2017, **5**, 2010–2017.

70 L. Luan, B. Tang, Y. Liu, W. Xu, Y. Liu, A. Wang, *et al.*, Direct synthesis of sulfur-decorating PAMAM dendrimer/mesoporous silica for enhanced Hg(II) and Cd(II) Adsorption, *Langmuir*, 2022, **38**, 698–710.

71 P. Bhunia, S. Chatterjee, P. Rudra and S. De, Chelating polyacrylonitrile beads for removal of lead and cadmium from wastewater, *Sep. Purif. Technol.*, 2018, **193**, 202–213.
72 M. E. Mahmoud, A. E. H. Abdou, M. E. Sobhy and N. A. Fekry, Solid–solid crosslinking of carboxymethyl cellulose nanolayer on titanium oxide nanoparticles as a novel biocomposite for efficient removal of toxic heavy metals from water, *Int. J. Biol. Macromol.*, 2017, **105**, 1269–1278.
73 Q. Zhou, Y. Huang, L. Liu, Z. Li, Y. Xiao, Z. Li, *et al.*, Enhanced Cadmium Adsorption by Silicate-Modified Biochar Derived from Sawdust: Mechanisms and Performance Analysis, *Surf. Interfaces*, 2025, 106430.
74 J. Li, D. Shan, Z. Gao, X. Zhang, Y. Xie, M. Huang, *et al.*, The adsorption characteristics and adsorption mechanism of magnesium- and ultrasound-modified rice straw biochars on cadmium in water, *J. Indian Chem. Soc.*, 2025, **102**, 102114.
75 Z. Wang, H. Deng, Y. Gao, S. Zhou, F. Zhou, G. Ye, *et al.*, Microwave acid treatment induces endogenous active adsorption sites in montmorillonite for cadmium immobilization in soil, *Appl. Clay Sci.*, 2025, **276**, 107939.
76 J. Datta and S. Deb, Tea factory waste as a cost-effective and sustainable cadmium(II) adsorbent: Investigating adsorption isotherms, kinetics, and thermodynamics, *Phys. Chem. Earth*, 2025, **140**, 104042.
77 C. Vázquez-Mendoza, R. Leyva-Ramos, N. A. Medellín-Castillo, D. H. Carrales-Alvarado and A. Aragón-Piña, Cadmium(II) removal from aqueous solution by adsorption on water hyacinth (*Eichhornia crassipes*) hydrochar modified with citric acid, *Case Stud. Chem. Environ. Eng.*, 2025, **12**, 101267.
78 M. Li, M. Y. Li, C. G. Feng and Q. X. Zeng, Preparation and characterization of multi-carboxyl-functionalized silica gel for removal of Cu (II), Cd (II), Ni (II) and Zn (II) from aqueous solution, *Appl. Surf. Sci.*, 2014, **314**, 1063–1069.
79 H. M. A. Hassan, M. S. Alhumaimess, I. H. Alsohaimi, A. A. Essawy, M. F. Hussein, M. H. Alshammari, *et al.*, Biogenic-mediated synthesis of the Cs2O-MgO/MPC nanocomposite for biodiesel production from oliver oil, *ACS Omega*, 2020, **5**, 27811–27822.
80 T. U. D. Thi, T. T. Nquyen, Y. D. Thi, K. H. Ta Thi, B. T. Phan and K. N. Pham, Green synthesis of ZnO nanoparticles using orange fruit peel extract for antibacterial activities, *RSC Adv.*, 2020, **10**, 23899–23907.
81 L. Huang and J. G. Lu, Synthesis, Characterizations, and Applications of Cadmium chalcogenide nanowires: a review, *J. Mater. Sci. Technol.*, 2015, **31**, 556–572.
82 R. Kumar, P. Bhargava and A. Dvivedi, Synthesis and Characterization of A New Cadmium Complex, Cadmium [(1,10-phenanthroline) (8hydroxyquinoline)]Cd(Phen)q, *Procedia Mater. Sci.*, 2015, **10**, 37–43.
83 D. Singhwal and P. S. Rana, Cadmium oxide nanoparticles doped with nickel and silver: photocatalytic activity for environmental remediation, *Mater. Chem. Phys.*, 2024, **314**, 128895.
84 K. S. W. Sing, D. H. Everett, R. A. W. Haul, L. Moscou, R. A. Pierotti, J. Rouquerol, *et al.*, Annexes: IUPAC recommendations: reporting physisorption data for gas/solid systems, *Handb. Heterog. Catal.*, 2008, **3–5**, 1503–1516.